

Huang Guo-chin Dino (Orcid ID: 0000-0002-2563-737X)

Savvaidis Alexandros (Orcid ID: 0000-0001-6373-5256)

Walter Jacob, I. (Orcid ID: 0000-0001-7127-9422)

## Mapping the 3-D Lithospheric Structure of the Greater Permian Basin in West Texas and Southeast New Mexico for Earthquake Monitoring

Guo-chin Dino Huang<sup>1\*</sup>, Alexandros Savvaidis<sup>1</sup>, and Jacob I. Walter<sup>2</sup>

<sup>1</sup>Bureau of Economic Geology, The University of Texas at Austin, Austin, Texas, United States.

<sup>2</sup>Oklahoma Geological Survey, University of Oklahoma, Norman, Oklahoma, United States.

\*Corresponding author: Guo-chin Dino Huang (dino.huang@beg.utexas.edu)

### Key Points:

- A statewide, earthquake-monitoring network has been established in Texas.

This article has been accepted for publication and undergone full peer review but has not been through the copyediting, typesetting, pagination and proofreading process which may lead to differences between this version and the Version of Record. Please cite this article as doi: 10.1029/2019JB018351

- We developed a tomographic velocity model for much of West Texas and southeast New Mexico for the purpose of earthquake monitoring.
- Distribution of the  $V_p/V_s$  ratio shows basin-scale features that suggest high pore-fluid pressure existing in the Greater Permian Basin.

## Abstract

The Greater Permian Basin is not only a complex tectonic regime, but it has also been and continues to be a productive oilfield where the seismicity rate in the basin has significantly increased since 2008. Since 2015, our understanding of the seismogenesis in the basin has increased owing to the establishment of a statewide seismic network known as TexNet for monitoring earthquake activities.

A crucial component of improving the accuracy of the hypocentral location is an accurate velocity model that can better confirm the existing regional tectonic regime. We collected data from current TexNet operations and previously deployed seismic arrays and performed a joint local and teleseismic earthquake tomographic inversion, resulting in a 3-D tomography model for earthquake monitoring.

The preferred 3-D tomography model includes a prominent feature at a depth range of 0–20 km, where distinct lower wave-speed anomalies overlap with the surface trace of the Delaware Basin.

These anomalies suggest a basin-scale lithological difference from surrounding regions and corroborate basin characteristics. Findings also suggest that the Midland Basin may be more lithologically uniform than the Delaware Basin. A strong correlation exists between dense seismicity clusters and the obtained lower  $V_p/V_s$  ratios. Four significant clusters having  $V_p/V_s$  ratios ranging from 1.689 to 1.720 were identified. Using the  $V_p/V_s$  ratio as a proxy to evaluate the state of the pore-fluid pressure, we think this spatial correlation suggests that the Greater Permian Basin currently comprises overpressurized fluid-filled host rocks.

## Plain Language Summary

Since 2017, a new statewide earthquake monitoring network, known as TexNet, has detected several active seismic zones in Texas. Among them, the Greater Permian Basin has a strong earthquake occurrence rate. In order to provide a better velocity model for the area of study, we followed two steps. First, on the basis of TexNet data from early 2017, we developed a 1-D velocity model to account for the local geology better than the average Earth model does. A localized 1-D model was thus adapted from this work. In this model, a subsurface layer with slower P-wave speed is suggested to corroborate the regional tectonic setting as a sedimentary basin. Second, in late-2018, on the basis

of the previous work, we collected more data and expanded the study area to cover the whole Greater Permian Basin. The resulting 3-D tomography model features lower  $V_p/V_s$  ratios, indicating that currently the pore-fluid pressure is high in the basin.

## 1. Introduction

Located in an area across West Texas and southeast New Mexico, the Greater Permian Basin consists of three major geologic units—the Delaware Basin, the Midland Basin, and the Central Basin Platform (Figure 1). All three features are underlain by a Precambrian basement and the Ellenburger Formation at the very bottom of these geologic units. The thickness of sediments varies across the Greater Permian Basin, where it can be as thick as 7 km in the Delaware Basin and as thin as 3 km in the Midland Basin (Doser et al., 1992).

Industrial activities (e.g., hydrocarbon extraction and wastewater injection) have been conducted in the Greater Permian Basin since the 1920s (Frohlich et al., 2016), and to date oil production still continues across the region. Since then, although the occurrence rate of felt earthquakes (e.g.,  $ML > 3$ ; see <https://earthquake.usgs.gov/monitoring/anss>) in the Greater Permian Basin is relatively low, earlier studies have determined that several, if not all, seismicity clusters are linked to industrial activity, such as reservoir production and enhanced recovery operations (Rogers & Malkiel, 1979), whereas other seismicity clusters have been associated with tectonic causes (e.g., migration of naturally overpressurized formation fluids and tectonic activities). For example, a few periods of swarm-type earthquakes have been identified using a temporary seismograph network (Rogers & Malkiel, 1979) in the Delaware Basin, with a local magnitude ( $ML$ ) ranging between 0 and 3, which can be attributed to high-pressurized fluid injection that resulted in high pore pressure near faults. Recently the number of felt earthquakes ( $ML > 3$ ) in Texas has risen from 2 events/yr before 2008 to 12 events/yr after 2008 (Frohlich et al., 2016)—a rise that has drawn public attention. A statewide earthquake-monitoring system, known as TexNet, which was funded in 2015, began deploying stations in late 2016 (Savvaidis et al., 2019). It currently operates 24 permanent and 75 portable new stations across Texas. The additional stations have enhanced the system's ability to detect microseismicity across Texas, and to date TexNet has reported more than 6,000 small

earthquakes (e.g.,  $M_L < 3$ ; see <http://www.beg.utexas.edu/texnet-cisr/texnet/earthquake-catalog>) since January 2017.

Among several newly detected seismic zones in Texas, the Greater Permian Basin has a higher earthquake occurrence rate than other adjacent seismic zones in the region. However, its complex geologic structure constitutes a challenge for TexNet to locate the earthquakes' precise hypocentral depths in the basin. For example, in the Delaware Basin, using the IASP91 model (Kennett & Engdahl, 1991) to locate earthquakes shows the depth range of detected seismicity to be from the subsurface down to around 14 km, whereas some hypocenters were clustered at 0 km depth, which cannot be realistic. Such unrealistic focal depths imply that the earthquakes in the Delaware Basin are at a relatively shallower depth, but the IASP91 model provides poor vertical constraints on focal depths. An effort has been put in place to resolve this issue with the development of a minimum 1-D velocity model to account for the local geology better than the IASP91 model does (e.g., Huang et al., 2017). In previous work, we utilized initial hypocentral information determined using TexNet's routine process to further relocate these earthquakes using the double-difference relocation method (i.e., hypoDD; Waldhauser & Ellsworth, 2000). At the same time, we employed statistical regression (i.e., Wadati, 1928) to constrain the origin times of these hypoDD-relocated earthquakes. The constrained origin times and hypoDD-relocated earthquake hypocenters, along with velocity information of the subsurface from a local sonic-log profile, were used in tomographic inversion to update the crustal velocity model for the Delaware Basin, and a new 1-D model was thus adapted from these tomography results. As expected, we found that both local topography and subsurface structures have a very strong influence on locating earthquakes that occurred at a very shallow depth range (e.g.,  $< 5$  km) in the Delaware Basin. A subsurface layer having a  $V_p$  as low as 3.5 km/s is suggested to be present in order to corroborate the regional tectonic setting as a sedimentary basin (Huang et al., 2017; Savvaidis et al., 2019; referred to as the *DB1D model* hereafter).

Although the DB1D model has taken the local geology into account, the velocity model still needs improvement to better interpret the complex 3-D heterogeneity of the Greater Permian Basin. In this paper, we present results of a follow-up study that is based on that of Huang et al. (2017) to combine data from both current TexNet and the temporary seismic arrays that were previously

deployed in the Greater Permian Basin (e.g., *the Transportable Array [TA]*; the *SIEDCAR array*, Rockett et al., 2010). We attempt to develop a higher resolution 3-D velocity model by including more local and teleseismic data from both seismic networks. Inclusion of these data increases ray-crossing coverage within the volume of the velocity model, resulting in better model resolution.

## 2. Data Processing and Analysis Techniques

We collected local/regional earthquake data from TexNet (2017/01–2018/11), the TA (2008–2010), and the SIEDCAR (2008–2010) and used teleseismic earthquake data recorded by the TA (2008–2010) only (Figure 2). For TexNet data, the selection of local/regional earthquake phase arrivals was based on the TexNet earthquake catalog (<http://www.beg.utexas.edu/texnet-cisr/texnet/earthquake-catalog>). In addition, we performed earthquake detection using the TA and SIEDCAR data for 2008–2010. In a way similar to that of other recent studies in Texas (e.g., Walter et al., 2016, 2018), we detected the signal triggers and automatically associated event locations using standard short-time average/long-time average (STA/LTA) algorithms and an automatic associator, which identifies an expected possible earthquake on the basis of 1-D traveltimes lookup tables. Because it requires only four stations for an event to be associated, false-positive earthquake detection might be created, so we manually reviewed each earthquake, adjusted the automatic phase picks, and added phase picks as needed. Manual review was also necessary because STA/LTA algorithms did not always trigger on *S*-phases owing to the low signal-to-noise ratio on horizontal components at regional distances. The final step for processing the TA and SIEDCAR data was locating the earthquakes using a local 1-D velocity model (e.g., the DB1D model) in order to acquire preliminary events' origin times and hypocenters.

Different approaches were applied when processing local/regional and teleseismic data. For phase identification of local/regional earthquakes, we picked phase arrivals using various filter bands to remove background noise to assure the quality of phase picking (Figure 3). To mitigate the bias introduced from possible misidentification on first arrivals, in addition to using appropriate weights, we empirically avoided using local/regional phase arrivals from stations at epicentral distances greater

than 300 and 200 km for *P*- and *S*-arrivals, respectively. For each local/regional earthquake, a minimum of three *P*- and two *S*-arrivals is needed to perform hypocenter relocation at each iteration. Upon combining all available data sets, we used a total of 56,674 *P*-arrivals and 46,122 *S*-arrivals picked from 4,488 local/regional earthquakes. We based teleseismic events on the Advanced National Seismic System (ANSS) catalog (e.g., <https://earthquake.usgs.gov/monitoring/anss>) in selecting 36 teleseismic earthquakes with  $M > 7$  at a distance range of between  $30^\circ$  and  $90^\circ$ . After accessing the data quality using waveform cross-correlation, we selected a total of 1,689 qualified teleseismic *P*-arrivals.

Next we parameterized the model volume in the spherical coordinate so as to mitigate the Earth's curvature effects over the large area, which covers the Greater Permian Basin, extending across West Texas to southeast New Mexico. The volume dimension is 800 km (east–west)  $\times$  720 km (north–south)  $\times$  84 km (vertical), in which zero-depth is assigned to be mean sea level (MSL) and the top of the volume is placed at 4 km above MSL. Because the top limit of the model is higher than the highest station (at an elevation of 2,078 meters) in our study area, traveltimes computation could thus account for the differences in station elevation by embedding the stations within the model volume. Since we are not interested in the very deep part of the lithosphere, the bottom of the model is set at 80 km depth to cover the area of interest adequately. Because of the lack of deeper local/regional earthquakes (e.g., deeper than Moho depth) that occurred in our study area, imaging of the deeper parts of the model volume relied heavily on teleseismic *P*-arrivals. As a result, raypath densities in the deep and shallow parts of the model were therefore uneven. We attempted to balance the sensitivities of the model parameters to data distribution, which is somewhat influenced by the size of grid spacing. In particular, we tried to retain vertical sensitivity to the velocity structure of the Greater Permian Basin using very fine vertical grid spacing. Computation cost was also taken into account when the model was parameterized. After testing several choices of grid spacing, we selected a horizontal spacing of 20 km and a vertical spacing of 2 km.

A well-constrained starting model could reduce possible bias introduced from undersampled nodes in the model volume and lead to faster solution convergence. We therefore collected available subsurface seismic measurements (e.g., sonic logs or vertical seismic profiles) and took them into

account when determining the starting model for tomographic inversion, thus providing ourselves with a realistic constraint on subsurface structures. These measurements were taken from different locations across our study area, provided by the industrial associates of the Center for Integrated Seismicity Research (CISR), which is affiliated with the Bureau of Economic Geology, The University of Texas at Austin. At the same time, we used the regression method known as the Wadati diagram (Figure 4) approach to estimate the  $V_p/V_s$  ratio, which resulted in a  $V_p/V_s$  ratio of 1.75 for constructing the starting  $V_s$  model. In general, these borehole seismic profiles were sampled at a very fine grid spacing (e.g., as small as 0.5 ft—the equivalent of 0.1524 m), dropping to as much as 3 km below MSL. The measurements commonly presented a slower  $P$ -wave speed of 2–3 km/s between local ground surface and MSL. Note that the wave speed is generally slower than that of our DB1D model at a similar depth range. Nevertheless, on the basis of these measurements, we generated two starting models to test the sensitivity of inversion to the subsurface structures within the starting models. These starting models are (1) the DB1D model and (2) the modified DB1D model (Figure 5), in which the speeds of both  $P$ - and  $S$ -waves are reduced by 20% from those of the DB1D model for nodes at 0- and 2-km depths. In the two starting models, the Moho depths are set to be 38 km below MSL on the basis of receiver function analysis (Crotwell & Owens, 2005). We allowed the Moho to be adjusted during the course of inversion.

Using the joint data set and two starting models, we performed tomographic inversion using a nonlinear iterative algorithm (Roecker et al., 2004, 2006) to invert for a 3-D velocity structure. The traveltimes tables used in earthquake relocation and seismic ray tracing within the model volume were constructed using a spherical adaptation of the finite-difference Eikonal solver (e.g., Hole & Zelt, 1995; Zhang et al., 2012). Relocating hypocenters of local/regional earthquakes is part of the inversion procedure and we used the adjusted model in each iteration, in which a grid-search approach is implemented to achieve a global minimum of traveltimes misfit. Although the earthquake relocation is performed in a step separated from ray tracing, we added the hypocenter terms into the system of linear equations explicitly and later the hypocentral perturbation will be solved simultaneously with velocity parameters. This approach could optimize the inversion and mitigate solution bias of velocity parameters introduced from mislocated hypocenters (Roecker et al., 2006).

In order to mitigate the effects introduced from Earth's structural anomalies located outside the regional model volume, we minimized traveltimes of teleseismic earthquakes in a relative manner. We also avoided using teleseismic *S*-waves as we considered that, compared to teleseismic *P*-waves, teleseismic *S*-waves tend to be affected more by the anomalies existing in the upper mantle outside our study area. The treatment on teleseismic *P*-wave data involves determination of the entry point at the bottom of model volume for the teleseismic rays. For a given teleseismic ray, the total traveltime is a sum of (1) the time,  $t_1$ , from the hypocenter to the base of the model volume and (2) the time,  $t_2$ , from the teleseismic ray's entry point at the bottom of the model to the receiver. The teleseismic ray path is then determined by following the steepest wave speed gradient from the source to the receiver. The point at the bottom of the model volume that can result in a minimum traveltime (i.e., the sum of  $t_1$  and  $t_2$ ) will thus be considered the entry point. We first used the IASP91 model (Kennett & Engdahl, 1991) to determine the traveltime for a given teleseismic ray propagating from the source to a presumed point at the bottom of the model volume. After that, the traveltime for the propagation path from the presumed point to the seismic station was determined from the traveltime tables based on the previously inverted velocity model. The search of the entry point for the given teleseismic ray was iterated until the minimum traveltime was found. All local/regional and teleseismic earthquakes are then used to jointly perform ray tracing to form the system of linear equations.

In each iteration, perturbations to wave speeds within the model were determined using a weighted, damped least-squares algorithm (Paige & Saunders, 1982) that solved the system of linear equations formed from the raytracing of joint local/regional earthquakes and teleseismic sources. Seismic wave speeds were thus iteratively adjusted to minimize traveltime misfits between observations and predictions. Although  $V_p$  and  $V_s$  can be independently resolved, we inverted for *S*-wave speeds on the basis of  $V_p/V_s$  ratio values instead. The *S*-wave speeds were then converted back from the resulting  $V_p/V_s$  ratios for traveltime table construction in each iteration. The reason for this kind of approach is that we intend to compensate for the generally lower  $V_s$  resolution resulting from less accurate *S*-wave arrival times and avoid possible solution divergence for *S*-wave speeds.

### 3. Inversion Results and Assessment of Model Resolutions

We monitored the inversion to determine the optimal number of iterations required for solution convergence, which can be seen from the trade-off curve between data misfit and model improvement (Rawlinson & Sambridge, 2003). The shape of a trade-off curve is significantly influenced by two main regulators implemented in each iteration: the damping factor and smoothing criteria. The first serves the purpose to regulate the inversion to allow solutions to be found for ill-posed problems and to suppress possible overstepped perturbations in model parameters when solving the system of linear equations. The latter is used before/after solving the system of linear equations, which is in pursuit of a geologically realistic model by removing abrupt changes at the boundaries of model parameters because the locations of those boundaries may be arbitrary. The smoothing approaches used in our inversion procedure include applying *a priori* gradient and posterior moving average of the model parameters. Our approach to achieving a stable convergence of tomographic inversion is similar to that described in Huang et al. (2009), Nunn et al. (2014), and Razi et al. (2016), and we tested several combinations of these factors. Although a small damping factor and the brevity of a moving window, even with no smoothing at all, can achieve convergence faster, it may nevertheless create artificial disturbances in tomographic images owing to an underdamped linear extrapolation. This effect can even be enhanced by these nodes with fewer rays passing through. In our study area, raypath distribution is denser around seismicity clusters but relatively sparse in the deeper parts of the model volume and in areas outside the United States, where no seismic stations are available (Figures 2). To mitigate this disadvantage owing to unsampled model parameters, throughout iteration steps, a covariance matrix was estimated and added to the system of linear equations to provide *a priori* gradient constraints. A smoother gradient can be estimated based on the wavespeeds of neighboring grids. In conjunction with an appropriate damper and posterior smoothing, we intend to restrict the velocity perturbation at each iteration to be small so as to achieve inversion stability.

While the inversion was iterated 82 times to ensure the convergence, the trade-off curve suggested that the model adjustments became modest at the 29th iteration (Figure 6). At the 29th iteration, the root mean square (RMS) misfit of both local/regional *P*- and *S*-arrivals combined has

been reduced by as much as nearly 33% (from 0.762 to 0.511 sec). Specifically, RMS *P*-residual dropped by around 24% (from 0.482 to 0.365 sec) and RMS *S*-residual misfit decreased by 35.4% (from 1.006 to 0.650 sec). From the starting 1-D model, the non-zero mean of *S*-residual seen from the histogram (Figure 6) indicates that *V*<sub>s</sub> needs to be increased (i.e., reducing the *V*<sub>p</sub>/*V*<sub>s</sub> ratio). Over the course of iteration, the peak of the histograms of *S*-residual moved toward zero-mean, which is indicative of being on the appropriate track of adjusting the *V*<sub>s</sub> model. We also found that with a smaller damper, inversion for *P*-wave-speed parameters converges faster than for *S*-wave-speed parameters. We believe that this result can be attributed to the much larger number of *P*-arrivals than *S*-arrivals (e.g., from combined local/regional and teleseismic earthquakes), as well as the appropriate estimate on the starting *V*<sub>p</sub> model.

Instead of constantly using a large damping value throughout iterations, we tested a series of damping values in each iteration that could best minimize the solution norm without overly suppressing model perturbation. This approach was found to reduce the number of iterations required for solution convergence and retain inversion stability at the same time. In addition to applying an optimal damper and covariance matrix estimation, we also incorporated posterior smoothing with  $\pm 2$  nodes in two horizontal directions and  $\pm 1$  node in the vertical direction through moving averages of perturbations at intermediate steps. We intended to make the wave-speed variation of neighboring nodes smoother while retaining the 3-D characteristics of velocity anomalies (e.g., wave-speed contrast). As we iterated the model, meanwhile, we compared results from the two starting models to examine the sensitivity of model parameters to the starting models. We found that resulting tomography patterns between the two starting models were generally similar, as the one taking seismic measurements into account resulted in much smoother images for shallower depths. This comparison suggests that our inversion scheme can reduce dependence on starting models and effectively resolve the inverse problem.

Resolution of model parameters (*V*<sub>p</sub> and *V*<sub>s</sub>) is related directly to the density of raypaths for ray-based seismic tomography. Within our study area, nodes that were close to earthquake clusters had a high number of raypath densities (e.g., at depths < 20 km in the Delaware Basin; Figure 7), whereas other nodes around the presumed Moho depth (38 km depth in the starting model for West

Texas; e.g., Crotwell & Owens, 2005) could still be mapped fairly well by refracted rays from local/regional earthquakes of the three clusters. However, in the southwest corner of the model volume, a number of nodes were without ray coverage owing to the absence of seismic stations. At a depth of 38–50 km, nodes were mapped by refracted rays from local/regional earthquakes and vertical teleseismic rays from the bottom of the model volume. Deeper than 50 km, resolution was controlled largely by teleseismic rays because of the absence of regional/local earthquakes in this depth range; hence, reduced resolutions were anticipated at these depths owing to reduced raypath densities. Nevertheless, the velocities of nodes within the crustal part of the model can be constrained by combining crossing local *Pg/Sg* phases, the crustal legs of near-vertically propagating *Pn/Sn*, and vertically propagating teleseismic *P*-waves.

We further performed a synthetic test (i.e., the checkerboard test) to verify model resolution by perturbing the resulting model parameters by  $\pm 3\%$  along a moving window. Using the perturbed velocity model and on the basis of the relocated hypocenters, we generated a data set of theoretical phase arrivals to perform the same inversion procedure as we did using true observations, which involved relocating earthquakes, to restore the checkerboard pattern (i.e., ground truth). We evaluated the resolution of model parameters by the state of pattern restoration as well as amplitude recovery. Figure 7 shows that recovery of the checkerboard patterns for both  $V_p$  and  $V_s$  largely corroborates the raypath-density distribution as we expected. Whereas the nodes with dense raypath coverage present reasonable recovery, the regions without seismic stations have no recovery at all. At the same time, amplitude restoration for the areas having high numbers of raypath densities is stronger than for those places having lower raypath densities. For example, within the area covered by the seismic stations, the amplitude recovery is stronger at 6 km depth than other depth-grid points. As implied by raypath-density distribution, recovery rate was reduced toward the deeper part of the model volume. It is worth noting that the recoveries of both amplitude and pattern for nodes at shallower depths (e.g., <8 km) are still reasonable, as all rays propagate in a nearly vertical angle to receivers at this depth range. We attribute the well recovery to a high number of passing rays received by densely distributed seismic stations in our study area.

On the basis of the assessment of both raypath densities and checkerboard-pattern recovery, we conclude that model parameters are (1) well resolved within the joint network at a depth range from subsurface down to 38 km depth, (2) less well resolved but still reasonably constrained in the central parts of the network to a depth of 38–50 km, and (3) poorly resolved below 50 km depth and in areas outside the United States.

## 4. Discussions

### 4.1 Tomographic images

We focused on tomographic images of parts above 38 km depth, where most  $V_p$  and  $V_s$  can be sampled simultaneously in the area of interest. As seen in map views, most prominent features in the model appear at a depth range between the subsurface and 20 km (Figures 8a and 8b), showing distinct lower wave-speed anomalies overlapping with the surface trace of the Delaware Basin (Figures 1 and 8a). This feature suggests a basin-scale lithological difference from that of the surrounding regions and corroborates basin characteristics. On the other hand, at the northeast corner of the model volume, a similar feature is not present at the same depth range for the Midland Basin, where higher wave-speed anomalies exist throughout the upper crust to depths greater than 20 km. Below a depth of 20 km, a higher wave-speed anomaly appears across the Greater Permian Basin.

In conjunction with map views, several cross sections were made to illustrate vertical variations of wave speed anomalies and  $V_p/V_s$  ratios across the Great Permian Basin. A southwest–northeast cross section (Figures 9 and 10a) perpendicular to the strike of the Delaware Basin shows strong vertical and lateral velocity variations. The lower wave-speed anomaly present at depths of 0–20 km beneath the Delaware Basin range is consistent with the one shown in Figure 8 at the same depth range. Across the Central Basin Platform from the same cross section and at the same depth range, higher wave-speed anomalies are broadly distributed beneath the Midland Basin range. Figures 10b–10c also illustrate three cross sections trending northwest–southeast that present three different

patterns in the Delaware Basin, the Central Basin Platform, and the Midland Basin, respectively. In cross section B, a body of lower wave-speed anomalies (at depths < 20 km) extends across West Texas and southeast New Mexico, consistent with features shown in Figures 8 and 10a.

Despite the fact that the predominate wave-speed contrast in our velocity model is still the Moho discontinuity, we discovered several minor velocity contrasts from the geometry of wave-speed contours at a depth of 0–20 km across the Greater Permian Basin (Figures 10a–10d). They present different patterns in the three subunits because they may indicate possible internal lithological boundaries within the Greater Permian Basin: in the Delaware Basin (Figure 10a), a distinct feature is shown by the contour of  $V_p = 6.4$  km/s across cross section B. The wave-speed geometry shows a degree of correlation with the wave-speed anomalies, and several minor wave-speed contrasts are identified: for example, the contour of  $V_p = 6$  km/s beneath the Delaware at 10–15 km depth under the Delaware Basin. Some wave-speed contrasts also fall in the same depth range of a strong  $V_p/V_s$  contrast in the Delaware Basin, suggesting a multilayer structure inside the Delaware Basin consistent with results of geologic mapping. In contrast, this feature is not clearly seen beneath the Central Basin Platform and the Midland Basin (Figures 10b and 10c), a difference in wave-speed patterns indicating that the Midland Basin is possibly more lithologically uniform than the Delaware Basin.

We further compared our tomographic velocity profiles with direct seismic measurement (e.g., sonic log data or vertical seismic profiles) (Figure 11) that were previously used to construct the starting model for the tomographic inversion. We extracted tomographic velocity profiles ( $V_p$  only) from neighboring grid points within the 40 km distance that surrounds the well locations of these seismic measurements. Despite the strong velocity gradient in these seismic measurements just above MSL, their overall patterns resemble our tomographic velocity profiles across our study area. We attribute this discrepancy to the difference in vertical grid spacing. Another possible cause is that these seismic measurements were taken along the borehole direction (i.e., vertical), whereas our seismic tomographic inversion resulted in an average velocity for each grid when we applied posterior smoothing.

#### 4.2 Interpretation of anomalous $V_p/V_s$ ratios

The ratio of compressional waves and shear waves (i.e.,  $V_p/V_s$ ) can be used as a proxy to characterize the lithosphere's petrophysical properties, such as porosity and the state of pore-fluid pressure (e.g., Dvorkin et al., 1999). Our tomographic inversion of  $V_p$  and  $V_p/V_s$  models offers an insight into petrophysical features of the Greater Permian Basin (see Figures 8, 10, and 12). Four significant clusters with  $V_p/V_s$  ratios ranging from 1.689 to 1.720, which are lower than those of the average 1-D  $V_p/V_s$  model, are identified. Within the earthquake clusters, low  $V_p/V_s$  ratios are distributed at a depth of 4–10 km, whereas the lowest  $V_p/V_s$  ratio (as low as 1.689) appears in the Delaware Basin. Although no boundaries are clearly defined to determine the volume of these anomalous bodies, a striking feature is that their apparent geometry seems to be geographically correlated with the Delaware and Midland Basins. Also note that the Central Basin Platform appears to separate these anomalies structurally.

Results of laboratory experiments indicate that the  $V_p/V_s$  ratio is dependent on several factors, such as rock composition (i.e., lithology) and pore-fluid pressure. A number of studies have suggested that porosity and pore-fluid pressure have a stronger influence (Dvorkin et al., 1999; O'Connell & Budiansky, 1974; Tatham, 1982), whereas other studies on lithospheric structures suggest that rock composition causes reduction in  $V_p/V_s$  ratios in their study areas (e.g., Li et al., 2018; Powell et al., 2010). Although the rock's composition appears to be a straightforward candidate for causing anomalous  $V_p/V_s$  ratios, as pointed out by Tatham (1982), the texture of the rock itself (e.g., porosity and crack/pore geometry) is a more predominant factor than lithology for influencing the  $V_p/V_s$  ratio. In fact, the two factors are somewhat coupled together. Christensen (1996) suggested that the amount of rocks' silica component is a decisive factor controlling both the Poisson's ratio and  $V_p/V_s$  ratio without taking the internal texture of the rock into account. From that study, the rock's silica component needs to increase to a predominant level (for example, 80%; e.g., Christensen, 1996; Powell et al., 2010), in which the rock type changes from sedimentary to igneous, to significantly reduce the  $V_p/V_s$  ratio. Under this scenario,  $P$ - and  $S$ - wave speeds are expected to respond differently to the lithological change. For example,  $V_p$  will decrease while  $V_s$  is increasing, or vice

versa. Based on a similar rationale, Powell et al. (2010) attributed the low  $V_p/V_s$  ratio observed in the New Madrid seismic zone to the presence of quartz-rich rock (i.e., granite) in which the high component of silica has significantly increased the  $V_s$  while  $V_p$  remains nearly unchanged; hence, the  $V_p/V_s$  dropped. A similar interpretation was made by Li et al. (2018), who observed a deep seismogenic zone featuring lower  $V_p/V_s$  ratio.

On the basis of the wave-speed variation of both  $V_p$  and  $V_s$  seen from our tomography results, we can expect a certain degree of lithological difference within the Greater Permian Basin. If the lithology does play a more decisive role than the rocks' internal textures on influencing the  $V_p/V_s$  ratio, that would be the case only when a body of volcanic intrusion is present in the basin range, especially at a very shallower depth range. Geological observation has indicated that the Delaware Basin consists of porous rocks (e.g., sandstone, carbonates, and shale) that contain a rich reserve of unconventional resources (natural gas and shale oil) and found no presence of igneous intrusion. Furthermore, the wave-speed variation of  $P$  and  $S$  waves apparently occurs in the same pattern (either decrease or increase) at a slightly different rate, which is contradictory to the cases that involved igneous intrusion. All of these observations suggest that lithological dependence is less significant than another plausible candidate—the physical state of pore fluid contained in the rocks—to influence the  $V_p/V_s$  ratios in the basin range.

Despite the fact that both fluid and gas saturation in the pore/crack may contribute to variations in  $V_p/V_s$  ratios, seismic  $P$ - and  $S$ -waves can react to the two factors differently. In particular,  $P$ -waves are much more sensitive to changes in pore-fluid pressure, whereas  $S$ -waves are more sensitive to the presence of liquid. Increasing pore-fluid pressure can more effectively reduce the rock's bulk modulus and further lower  $P$ -wave speed. On the other hand, the existence of liquid in the host rocks will lower  $S$ -wave speed by decreasing the shear modulus of the host rocks. Commonly, coexistence of overpressured liquid and gas can further complicate the variation in  $V_p/V_s$  ratios over regions. Nevertheless, this variation really depends on the combination of reduction rate of both  $P$ - and  $S$ -waves. They can be reduced either at the same or at an uneven rate. For example, in an overpressurized liquid-filled rock volume,  $V_p$  can drop faster than  $V_s$  because of excessive pore-fluid pressure, although  $V_s$  is affected by the presence of liquid as well (e.g., Nakajima et al., 2001; Takei,

2002). Despite the fact that  $V_p/V_s$  ratios resolved in our study area are not anomalously low (i.e., only at the level of 1.7), the agreement between their apparent patterns and the distribution of low-gravity anomalies suggests that the feature of lower  $V_p/V_s$  ratios is strongly associated with the content of a sedimentary basin characterized by porous and gas/fluid-saturated host rocks with a low density (e.g., Adams & Keller, 1996). A recent study by Drwiła et al. (2019) of  $Q_p$  and  $Q_s$  of the Delaware Basin provides additional evidence that  $V_p$  attenuates faster than  $V_s$  and further lowers the  $V_p/V_s$  ratio. Their results show that  $Q_p = 91$  and  $Q_s = 139$  for the entire Delaware Basin where the  $V_p/V_s$  ratio shown is commonly lower in our tomography model. Therefore, we consider that pressurized pore fluid within the formation is the most plausible candidate to simultaneously cause the reduction of  $V_p/V_s$  ratio and  $Q_p$  being smaller than  $Q_s$ .

#### 4.3 Seismicity and low $V_p/V_s$ ratios

A body of evidence indicates an association between highly clustered tectonic seismicity and anomalously low  $V_p/V_s$  ratios (e.g.,  $V_p/V_s < 1.7$ ) in many tectonic regimes (e.g., Bannister et al., 2006; Dahm & Fischer, 2014; Li et al., 2018; Lin and Shearer, 2009; Powell et al., 2010; Roecker et al., 2017). Other studies have also found that pressurized pore-fluid plays an important role in the occurrence of earthquake swarms in seismic zones (Hornback et al., 2016; Nakai et al., 2017; Shelly et al., 2013; Vidale & Shearer, 2006). As previously mentioned, the  $V_p/V_s$  ratio can be used as a proxy to represent the state of the pore-fluid pressure. In our study area, tomographically relocated earthquakes show several groups of clustered seismicity (Figures 8, 10, and 12), and some are highly concentrated in the area having lower  $V_p/V_s$  ratios. Although all seismicity in our study area is located at a range of 0–20 km depth in general, the depth extents vary across different clusters. In addition to seismicity in the two subbasins—the Delaware and Midland—other earthquake epicenters are scattered in the mountain range where  $V_p/V_s$  ratios are higher or at an average level. They tend to be distributed along the strike of the mountain range without clear clustering. The overall spatial distribution of earthquakes indicates that lower  $V_p/V_s$  ratios are independent of the presence of seismicity. One may argue that these anomalies may result from an unevenly distributed raypath

density; however, the synthetic tests have suggested that model parameters are reasonably resolved and their resolution is independent of the number of earthquakes within an area of interest. We believe that lower  $V_p/V_s$  ratios are more likely to be associated with the characteristics of a sedimentary basin, i.e., porosity and the content of the formations. The correlation between the two features—intense seismicity and low anomalies of  $V_p/V_s$  ratio—may offer an insight into the seismogenic nature of the Greater Permian Basin.

As the vast majority of earthquakes were highly concentrated in the area with lower  $V_p/V_s$  ratios, the low anomalies of  $V_p/V_s$  ratio in the four major seismicity clusters in fact present different degrees of spatial correlation with the seismicity (Figures 9 and 12). In zone 1, the depth range of seismicity broadly expands from the subsurface down to 20 km depth and depths fall into two major groups peaked at 2 and 8 km depths, where the lowest  $V_p/V_s$  is peaked around 6 km depth near the basement top. Although seismicity split into two apparent groups, they commonly occurred in areas with  $V_p/V_s$  lower than the background value. Furthermore, seismicity at depths of 6–20 km in zone 1 has most likely involved reactivation of pre-existing basement-rooted faults (see Figure 1 as well). In zones 2 and 4, most seismicity occurred in the basement. In zone 3, the depth correlation between low  $V_p/V_s$  anomalies and seismicity seems to be less significant than that for the Delaware Basin. The seismicity is mostly clustered at a shallower depth range of 0–4 km. It is noticeable that seismicity in zone 4 presents a strong lineation that is concentrated in the range of 6–12 km depths, revealing an unmapped pre-existing geologic structure (Figure 1) where the overall orientation of seismicity is parallel with the local direction of maximum horizontal shear stress (i.e.,  $SH_{max}$ , see panel A of Figure 13; Snee & Zoback, 2018). Of particular note is that in zone 4 there was no seismicity detected prior to 2017 (panel A of Figure 13). The earliest event detected was on August 14, 2017, by TexNet. Since then, the seismicity occurred at an average rate of 1 event per day, although the rate was as high as 9 events per day on November 23, 2018 (panels B and C of Figure 13). At the same time, the fluid injection in zone 4 started from 72<sup>nd</sup> month (with respect to January 2008) and the accumulative volume of injected wastewater significantly increased between the 102<sup>nd</sup> and 119<sup>th</sup> month. Although the injection volume was reduced before the outbreak of the seismicity, nevertheless, zone 4 remains seismically active to this date. On the basis of the agreement between the geometry of the seismicity

cluster and  $SH_{max}$ , we thus inferred that the elevated pore-fluid pressure resulted from fluid injection in this area may have favored the fault slip following the  $SH_{max}$  orientation.

Previous studies have suggested a link between industrial activities (e.g., oil production/enhanced recovery; Doser et al., 1992; Frohlich et al., 2016; Rogers and Malkiel, 1979) and seismicity in the Greater Permian Basin. Although some of the seismicity studied by Doser et al. (1992) is most likely to be tectonic related, evidence indicates increased pore-fluid pressure during gas production or enhanced oil recovery to have caused the seismicity in the Delaware Basin. Doser et al. (1991, 1992) also found that part of the Delaware Basin is tectonically overpressurized, contributing to the tectonic seismicity in West Texas. All seismicity they found associated with industrial activities is located in the area with lower  $V_p/V_s$  ratios revealed by our tomographic results. In the Midland Basin, previous studies suggest that seismicity in 1974–1982 was attributed to wastewater injection, whereas injection of pressurized carbon dioxide induced seismicity in 2006–2011 (Davis & Pennington, 1989; Gan & Frohlich, 2013). The role played by the injection here is that it reactivates the uncharted pre-existing faults by its supercritical pore-fluid pressure. Although the injected content was different, all these seismicities shared a seismogenic cause, i.e., increased pore-fluid pressure, and the location of injection sites was spatially correlated with seismicity clusters characterized by lower  $V_p/V_s$  ratios.

Although increased pore-fluid pressure may lead to immediate occurrence of induced seismicity near the injection wells, over time, the injected fluid should diffuse away from the injection site, altering seismic wave speed and further changing  $V_p/V_s$  ratios by elevated pore-fluid pressure. As a result, time-lag between fluid injection and outburst of seismicity is commonly seen. Given the complex geologic structure and long history of industrial activities in our study area, we consider that injection overpressure in shallow disposal intervals, natural overpressure in deeper reservoirs due to excessive overburden, and lots of distributed gas are the main factors in the Greater Permian Basin contributing to lowering  $V_p/V_s$  ratios. Because our tomographic images are accumulative results of all factors combined with no temporal constraints, however, differentiating whether the injected fluid was a predominant factor on the change of seismic wave speeds is difficult. Nevertheless, the spatial correlation between seismicity and lower  $V_p/V_s$  ratios indicates that regions characterized by lower

$V_p/V_s$  ratios (i.e., an indication of higher pore-fluid pressure) could be prone to occurrences of swarm-type seismicity, in which no clear mainshock-aftershock sequence pattern can be observed. Further study of the hydrogeological model for the Delaware Basin is needed.

## **5. Conclusion**

Using data from current TexNet, previously deployed TA, and SIEDCAR temporary arrays, we have resolved a 3-D lithospheric structure for much of West Texas and southeast New Mexico. Through the tomographic inversion, tightly clustered seismicity zones have been observed. Although the depth extent of these clusters varies, some of the seismicity may have involved the basement-rooted faults down to 12 km depth. At the same time, basin-scale characteristics of low  $V_p/V_s$  ratios are thus revealed from the tomographic images, suggesting that the Greater Permian Basin consists of geologic formations that may already have been pressurized. Furthermore, most relocated seismicity through tomography is distributed in regions having lower  $V_p/V_s$  ratios (as low as 1.689), indicating that the overpressurized Permian Basin is currently prone to occurrence of swarm-type earthquakes when the pore-fluid pressure is constantly disturbed.

## **Acknowledgments**

Our appreciation is going to S. W. Roecker of Rensselaer Polytechnic Institute for sharing his FDTomo algorithm as well as his extensive experiences on tomographic inversion. The authors would like to thank C. Breton and C. Lemon of the Bureau of Economic Geology, The University of Texas at Austin, for providing data for this manuscript, such as extraction of archived geologic data, drawing of the geological map, and compiling of information on fluid injection volume. Appreciation is also due H. Rodgers of the Bureau of Economic Geology, The University of Texas at Austin, for digitizing the analog vertical seismic profiles. We also like to thank B. Young, S. Whittaker, and P. Martone of the Bureau of Economic Geology, The University of Texas at Austin. Tomographic inversion cannot be done without their careful picks of phase arrivals. Seismic data of the Transportable Array used in this study were processed using SAC software. All maps were generated using GMT software

(Wessel & Smith, 1991). We also thank two anonymous reviewers for their constructive comments.

Funding for this work was provided by The State of Texas through the University of Texas Bureau of Economic Geology TexNet Seismic Monitoring and Research Project and the industrial affiliates of the Center for Integrated Seismicity Research (CISR). All seismic data used in this study can be downloaded from Incorporated Research Institutions for Seismology ([http://ds.iris.edu/SeismiQuery/by\\_network.html](http://ds.iris.edu/SeismiQuery/by_network.html)). All sonic logs and vertical seismic profiles were provided by the industrial affiliates of CISR.

## References

- Adams, D. C. & Keller, G. R. (1996), Precambrian basement geology of the Permian Basin region of West Texas and eastern New Mexico: A geophysical perspective, *AAPG bulletin*, 80, 410-431.
- Bannister, S., Thurber, C., and Louie, J (2006), Detailed fault structure highlighted by finely relocated aftershocks, Arthur's Pass, New Zealand. *Geophys. Res. Lett.*, 33, L18315, doi:10.1029/2006GL027462.
- Christensen, N. I. (1996), Poisson's ratio and crustal seismology, *J. Geophys. Res.*, 101, 3139-3156.
- Crotwell, H. P. & Owens, T. J. (2005), Automated receiver function processing, *Seismo. Res. Lett.*, 76, 702–708.
- Dahm, T. & Fischer, T. (2014), Velocity ratio variations in the source region of earthquake swarms in NW Bohemia obtained from arrival time double-differences, *Geophys. J. Intl.*, 196, 957-970.
- Davis, S. D. & Pennington, W. D. (1989), Induced seismic deformation in the Cogdell oil field of west Texas. *Bull. Seismo. Soc. Am.*, 79, 1477-1495.
- Doser, D. I., Baker, M. R., Luo, M., Marroquin P., Ballesteros L., Kingwell J., Diaz, H. L., and Kaip, G. (1992), The not so simple relationship between seismicity and oil production in the Permian Basin, west Texas, *Pure and Applied Geophysics*, 139, 481–506.

- Doser, D. I., Baker, M. R., and Mason, D. B. (1991), Seismicity in the War-Wink gas field, Delaware Basin, West Texas, and its relationship to petroleum production. *Bull. Seismo. Soc. Am.*, *81*, 971–986.
- Drwiła, M., Wcisło, M., Anikiev D., Eisner, L., and Keller, R. (2019), Passive seismic measurement of seismic attenuation in Delaware Basin, *The Leading Edge*, *38*, 138-143.
- Dvorkin, J., Mavko, G., and Nur, A. (1999), Overpressure detection from compressional- and shear-wave data, *Geophys. Res. Lett.*, *26*, 3417–3420.
- Ewing, T. E., Barnes, M. A., and Denison, R. E. (2019), Proterozoic foundations of the Permian Basin, West Texas and Southeastern New Mexico — a review, in *Anatomy of a Paleozoic Basin: The Permian Basin, USA, Volume 1.*, edited by S. C. Ruppel., 412pp.
- Frohlich, C., DeShon, H., Stump, B., Hayward, C., Hornbach, M., and Walter, J. I. (2016), A historical review of induced earthquakes in Texas, *Seismo. Res. Lett.*, *87*, 1022.
- Gan, W. & Frohlich, C. (2013), Gas injection may have triggered earthquakes in the Cogdell oil field, Texas, *Proceedings of the National Academy of Sciences*, *110*, 18786–18791.
- Hole, J. A. & Zelt, B. C. (1995), 3-D finite-difference reflection traveltimes, *Geophys. J. Int'l.*, *121*, 427-434.
- Hornbach, M. J., Jones, M., Scales, M., DeShon, H. R., Magnani, M. B., Frohlich, C., Stump, B., Hayward, C., and Layton, M. (2016), Ellenburger wastewater injection and seismicity in North Texas, *Phys. Earth Planet. Int.*, *261*, 54-68.
- Huang, G.-C. D., Aiken, C., Savvaidis, A., Young, B., and Walter, J. (2017), Improving the velocity structure in the Delaware basin of West Texas for seismicity monitoring, *Eos Trans. AGU*, S23C-0836.
- Huang, G.-C. D., Wu, F. T., Roecker, S. W., and Sheehan, A. F. (2009), Lithospheric structure of the central Himalaya from 3-D tomographic imaging, *Tectonophysics*, *475*, 524–543.
- Kennett, B. L. N. & Engdahl, E. R. (1991), Traveltimes for global earthquake location and phase identification, *Geophys. J. Int.*, *105*, 429-465.

- Li, Z., Ni, S., Roecker, S. W., Bao, F., Wei, X., and Yuen, D. A. (2018), Seismic imaging of source region in the 1976  $M_s$  7.8 Tangshan earthquake sequence and its implications for the seismogenesis of intraplate earthquakes, *Bull. Seismo. Soc. Am.*, *108*, 1302-1313.
- Lin, G. & Shearer, P. M. (2009), Evidence for water-filled cracks in earthquake source regions. *Geophys. Res. Lett.*, *36*, L17315, doi:10.1029/2009GL039098.
- Nakai, J. S., Weingarten, M., Sheehan, A. F., Bilek, S. L., and Ge, S. (2017), A possible causative mechanism of Raton Basin, New Mexico and Colorado earthquakes using recent seismicity patterns and pore pressure modeling, *J. Geophys. Res.*, *122*, 8051-8065.
- Nakajima, J., Matsuzawa, T., Hasegawa, A., and Zhao, D. (2001), Three dimensional structure  $V_p$ ,  $V_s$ , and  $V_p/V_s$  beneath northeastern Japan: implications for arc magmatism and fluids, *J. Geophys. Res.*, *21*, 843–21,857.
- Nunn, C., Roecker, S. W., Tilmann, F. J., Priestley, K. F., Heyburn, R., Sandvol, E. A., Ni, J. F., Chen, Y. J., Zhao, W., and the INDEPTH Team IV. (2014), Imaging the lithosphere beneath NE Tibet: teleseismic P and S body wave tomography incorporating surface wave starting models, *Geophys. J. Int'l*, *196*, 1724-1741.
- O'Connell, R. J. & Budiansky, B. (1974), Seismic velocity in dry and saturated cracked solids, *J. Geophys. Res.*, *79*, 5412–5426.
- Paige, C. C. & Saunders, M. A. (1982), LSQR: An algorithm for sparse linear equations and sparse least squares, *ACM Transactions on Mathematical Software*, *8*, 43–71.
- Powell, C. A., Withers, M. M., DeShon, H. R., and Dunn, M. M. (2010), Intrusions and anomalous  $V_p/V_s$  ratios associated with the New Madrid seismic zone. *J. Geophys. Res.*, *115*, doi:10.1029/2009JB007107.
- Rawlinson, N. & Sambridge, M. (2003), Seismic traveltime tomography of the crust and lithosphere. *Advances in Geophysics*, *46*, 81–197.
- Razi, A. S., Roecker, S. W., and Levin, V. (2016), The fate of the Indian lithosphere beneath western Tibet: Upper mantle elastic wave speed structure from a joint teleseismic and regional body wave tomographic study, *Physics of the Earth and Planetary Interiors*, *251*, 11–23.

- Rockett, C. V., Paulliam, J., and Grand, S. P. (2010), Seismic Tomographic Imaging of an Upper Mantle Anomaly beneath the Rio Grande Rift, *Eos Trans. AGU*, S31A-2028.
- Roecker, S. W., Ebinger, C., Tiberi, C., Mulibo, G., Ferdinand-Wambura, R., Mtelela, K., Kianji, G., Muzuka, A., Gautier, S., Albaric, J., and Peyrat, S. (2017), Subsurface images of the Eastern Rift, Africa, from the joint inversion of body waves, surface waves and gravity: investigating the role of fluids in early-stage continental rifting, *Geophys. J. Int'l*, *210*, 931-950.
- Roecker, S. W., Thurber, C., and McPhee, D. (2004), Joint inversion of gravity and arrival time data from Parkfield: New constraints on structure and hypocenter locations near SAFOD drill site, *Geophys. Res. Lett.*, *31*, doi:10.1029/2003GL019396.
- Roecker, S. W., Thurber, C., Roberts, K., and Powell, L. (2006), Refining the image of the San Andreas Fault near Parkfield, California using a finite difference travel time computation technique, *Tectonophysics*, *426*, 189-205.
- Rogers, A. M. & Malkiel, A. (1979), A study of earthquakes in the Permian Basin of Texas-New Mexico, *Bull. Seismo. Soc. Am.*, *69*, 843-865.
- Savvaidis, A., Young, B., Huang, G.-C. D., and Lomax, A. (2019), TexNet: A Statewide Seismological Network in Texas, *Seismol Res. Lett.*, <https://doi.org/10.1785/0220180350>
- Shelly, D. R., Moran, S. C., and Thelen, W. A. (2013), Evidence for fluid-triggered slip in the 2009 Mount Rainier, Washington earthquake swarm, *Geophys. Res. Lett.*, *40*, 1506–1512.
- Snee, J.-E. L. & Zoback, M. D. (2018), State of stress in the Permian Basin, Texas and New Mexico: Implications for induced seismicity, *The Leading Edge*, *37*, 127-134.
- Takei, Y. (2002), Effect of pore geometry on Vp/Vs: from equilibrium geometry to crack, *J. Geophys. Res.*, *107*, 2043, doi:10.1029/2001JB000522.
- Tatham, R. H. (1982), Vp/Vs and lithology, *Geophysics*, *47*, 336-344.
- Vidale, J. E. & Shearer, P. M. (2006), A survey of 71 earthquake bursts across southern California: Exploring the role of pore fluid pressure fluctuations and aseismic slip as drivers, *J. Geophys. Res.*, *111*, B05312, doi:10.1029/2005JB004034.
- Wadati, K. (1928), Shallow and deep earthquakes, *Geophys. Magazine*, *1*, 161-202.

Waldhauser, F. & Ellsworth, W. L. (2000), A double-difference earthquake location algorithm:

Method and application to the northern Hayward fault, California, *Bull. Seismo. Soc. Am.*, 90, 1353-1368.

Walter, J. I., Dotray, P. J., Frohlich, C., and Gale, J. F. W. (2016), Earthquakes in Northwest Louisiana and the Texas–Louisiana Border Possibly Induced by Energy Resource Activities within the Haynesville Shale Play, *Seismo. Res. Lett.*, 87, 285–294.

Walter, J. I., Frohlich, C., Borgfeldt, T., and Gerzina, J. (2018), Natural and induced earthquakes in the Texas and Oklahoma Panhandles, *Seismo. Res. Lett.*, doi: <https://doi.org/10.1785/0220180105>

Wessel, P., & Smith, W. H. F. (1991). Free software helps map and display data, *Eos Trans. AGU*, 72, 441.

Zhang, H., Roecker, S. W., Thurber, C. H., & Wang, W. (2012). Seismic imaging of microblocks and weak zones in the crust beneath the southeastern margin of the Tibetan plateau, In: Dar, I.A. (Ed.), *Earth Sciences*. InTech, Croatia.

**Figure captions:**

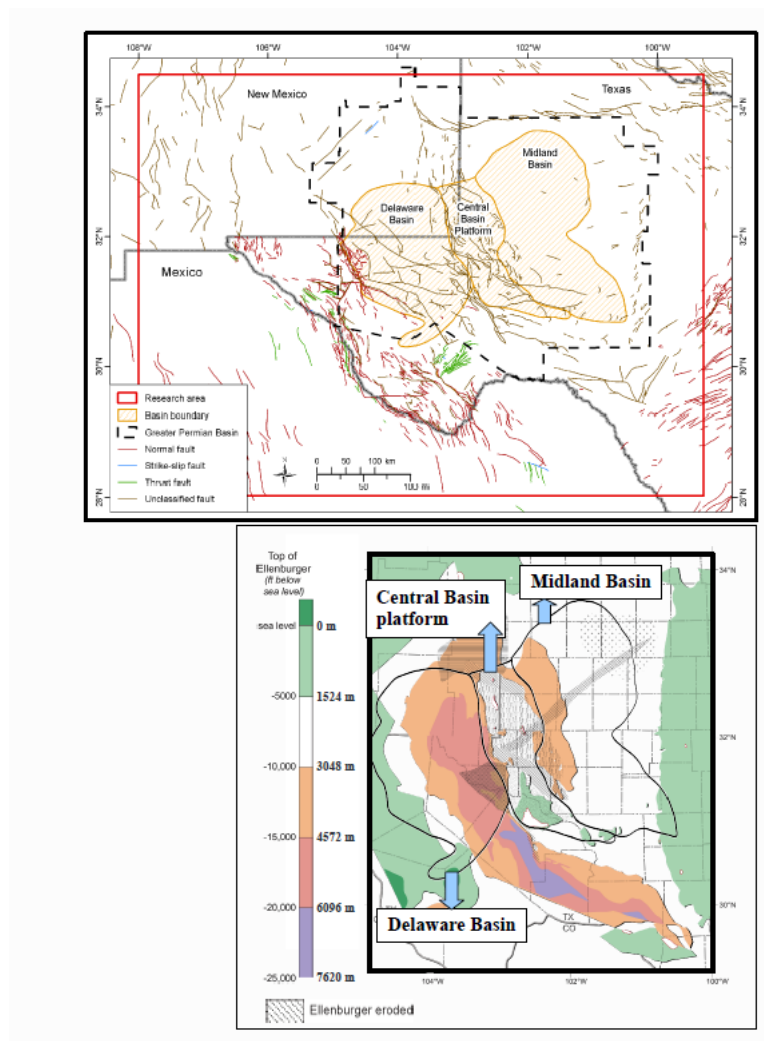


**Figure 1.** Regional tectonic map of study area. (Upper panel) Red line = study-area boundary spanning West Texas, southeast New Mexico, and part of Mexico. Study area contains major geologic unit—Greater Permian Basin—bounded by dashed black line and consisting of three major subunits (Delaware Basin, Central Basin Platform, and Midland Basin). Fault systems are well developed within the Delaware Basin and Central Basin Platform, whereas mapped fault traces are fewer in the Midland Basin; (Lower panel) Depth of the top of Ellenburger Formation across the Greater Permian Basin, modified from Ewing et al. (2019), used as proxy to represent the depth to the basement top. The depth varies across the basin: it is as deep as 6.1 km in the Delaware Basin, whereas it is shallower in the Midland Basin.

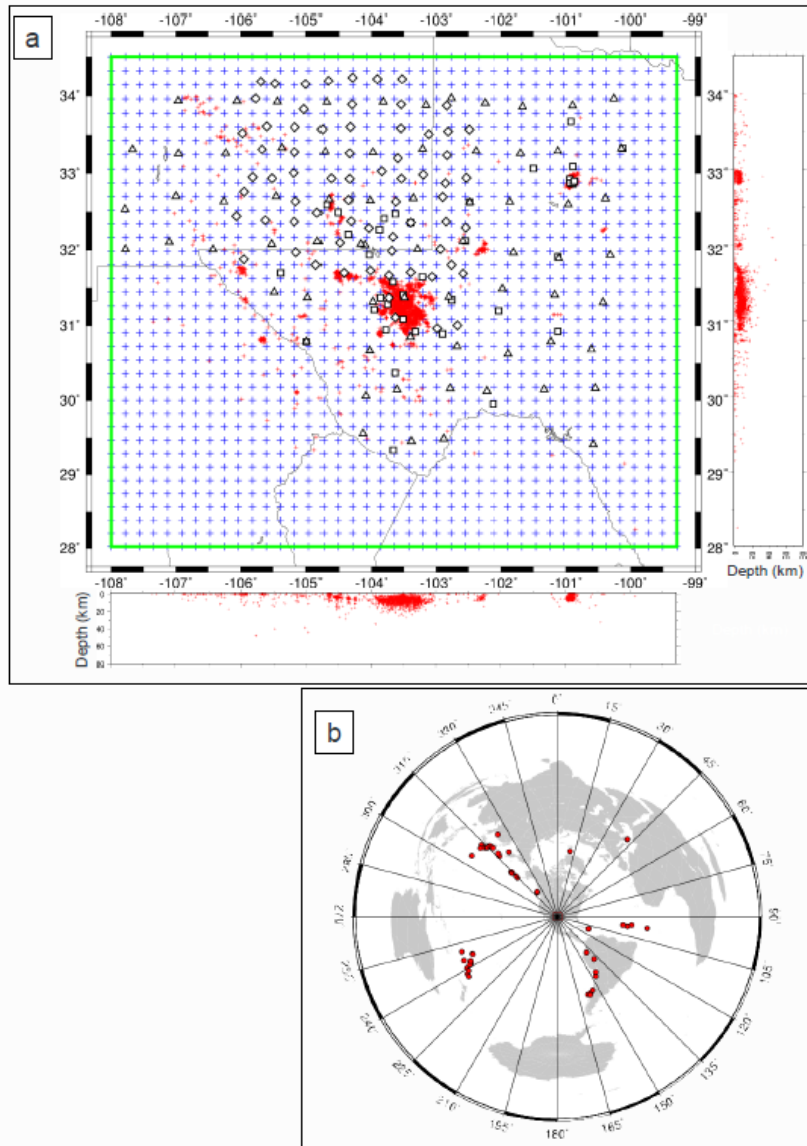


**Figure 2.** Seismicity distribution and seismic stations in study area. (a) Local and regional earthquakes— composite data set of TexNet (2017/01–2018/11), Transportable Array (2008–2010), and the SIEDCAR project (2008-2010); red crosses = earthquake epicenters. On map, blue crosses = tomographic inversion nodes, with 20-km spacing. White triangles, squares, and diamonds = seismic stations used in tomographic inversion—triangle = Transportable Array; square = TexNet; diamond = SIEDCAR. (b) Earthquakes at teleseismic range (30°–90° of great arc distance) to study area.

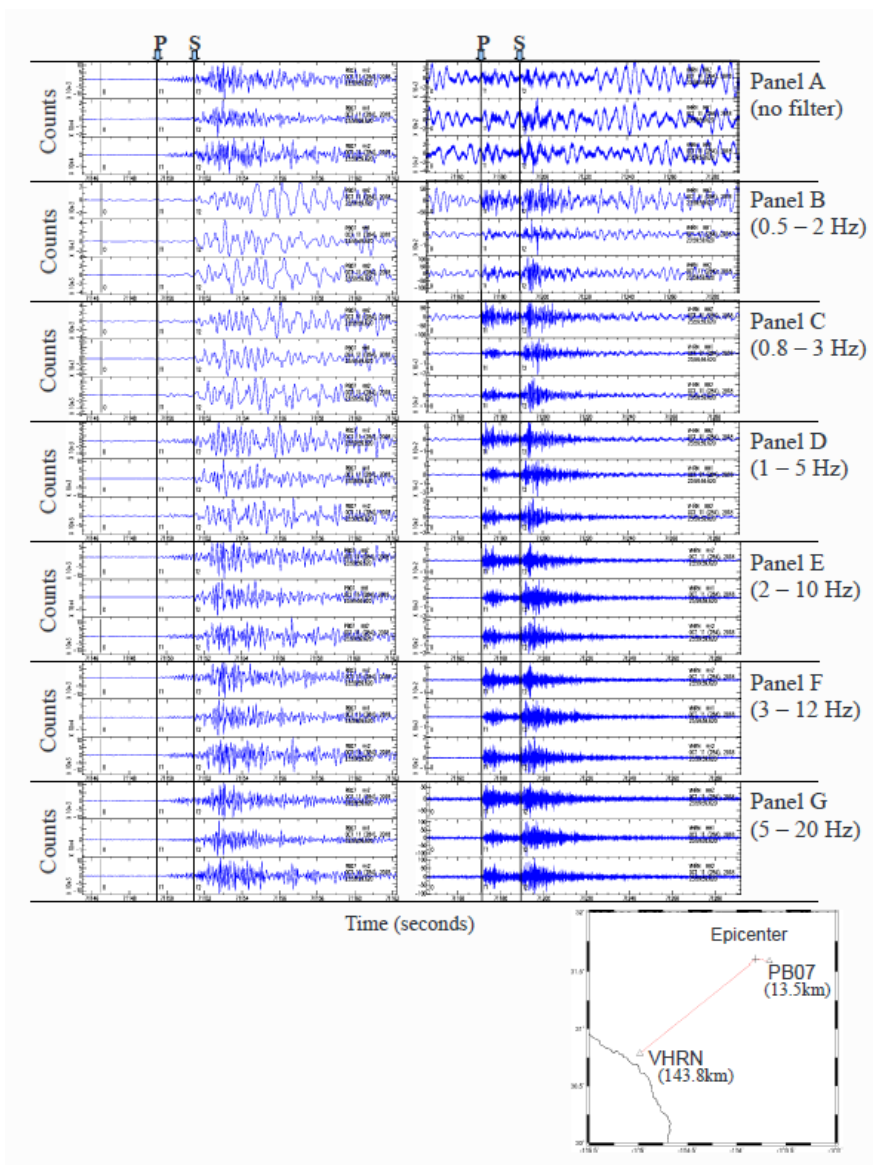


**Figure 3.** Example seismograms recorded by two TexNet seismic stations for an earthquake ( $M_L = 2.1$ ) that occurred on October 12, 2018. Lower right panel locates the earthquake epicenter and the two seismic stations. Six different filter bands (panels B–G; panel A = the original seismogram without filtering) were used to remove background noise and to assure the quality of phase picking. Letters P and S marked on top of the seismograms denote the first arrivals of P-wave and S-wave, which can be seen across all filtered seismograms. See text for details.

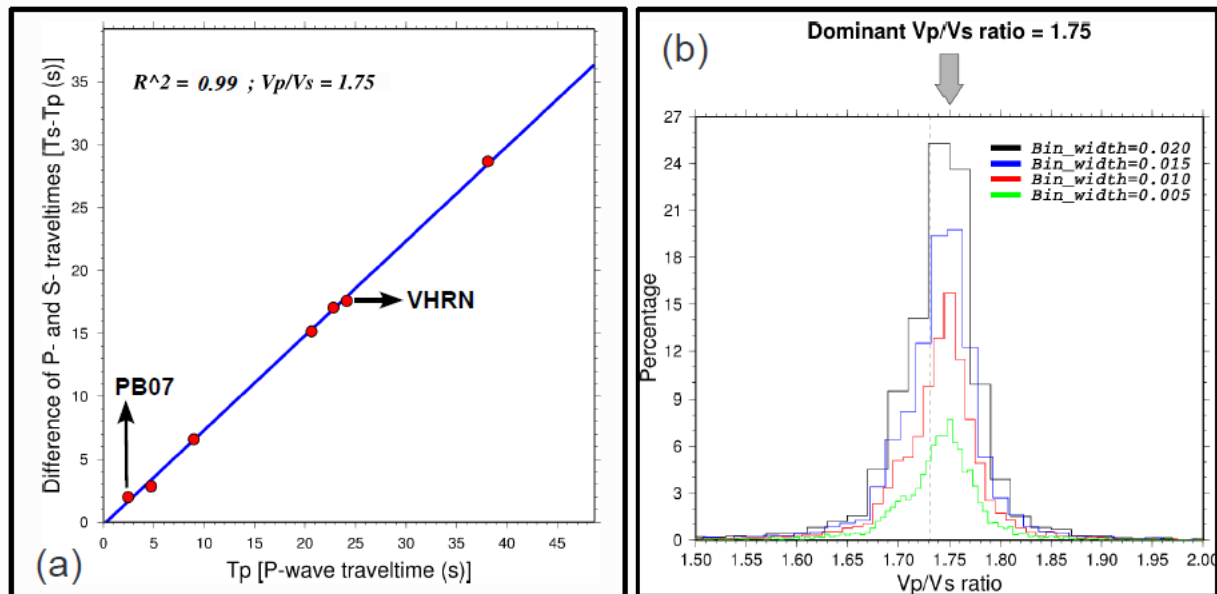


**Figure 4.** Panel (a): The Wadati diagram used to estimate the  $V_p/V_s$  ratio and assess the quality of phase picking for the example event shown in Figure 3. Red circles denote seismic stations used in phase picking. Correlation coefficient of 0.99 suggests the quality of phase picking; Panel (b): Statistical histogram of  $V_p/V_s$  ratio derived from the Wadati diagrams for all local/regional events used in the tomographic inversion. As a result, the dominant  $V_p/V_s$  ratio of 1.75 is used to construct a 1-D starting model.

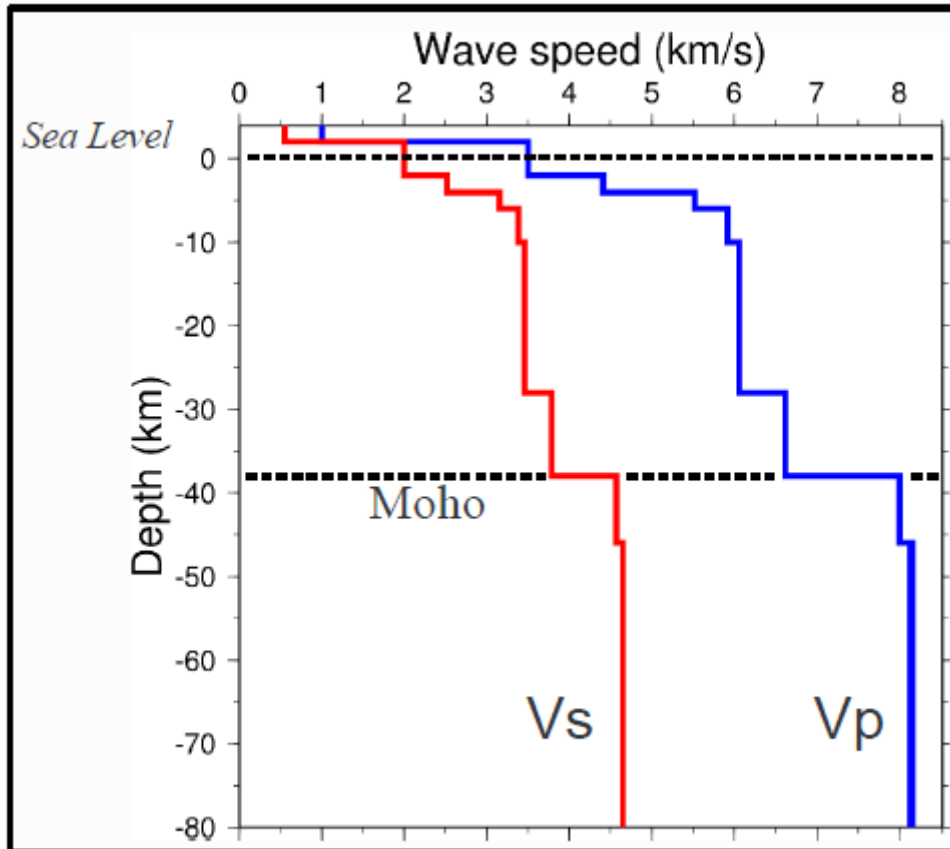


**Figure 5.** 1-D starting model (modified from Savvaidis et al., 2019) for tomographic inversion, with 2-km vertical spacing. We referred to that from Savvaidis et al. (2019) and a number of vertical seismic profiles to construct the 1-D starting model, for which  $V_s = V_p/1.75$ , and the Moho is set to be at 38 km depth (e.g., Crotwell & Owens, 2005). See text for details.

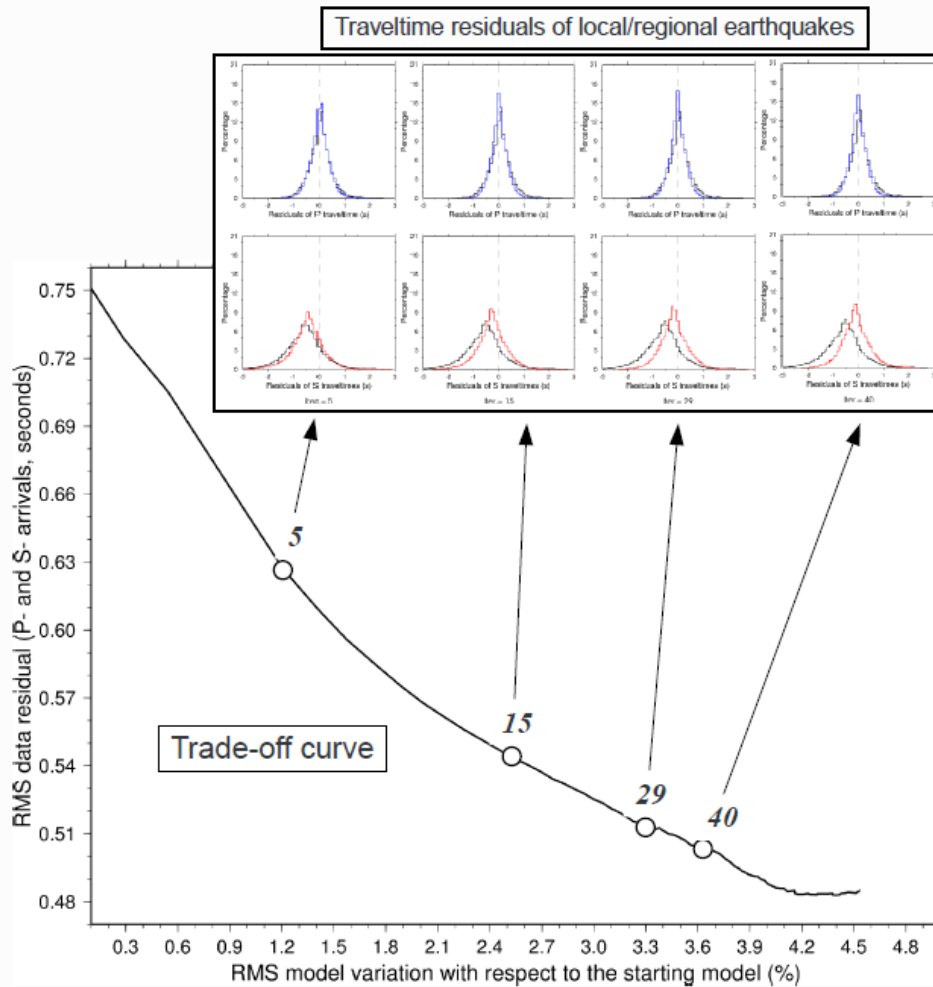
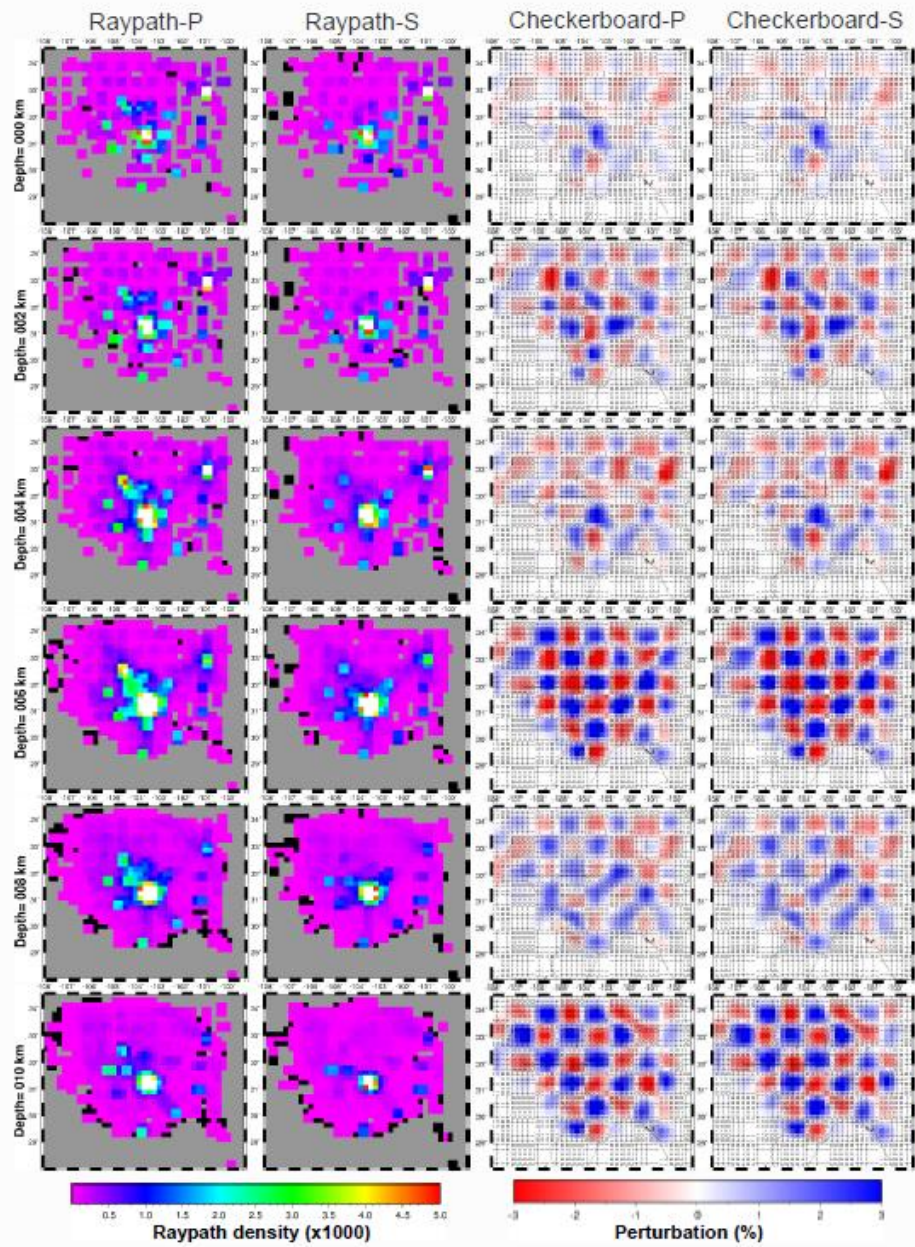
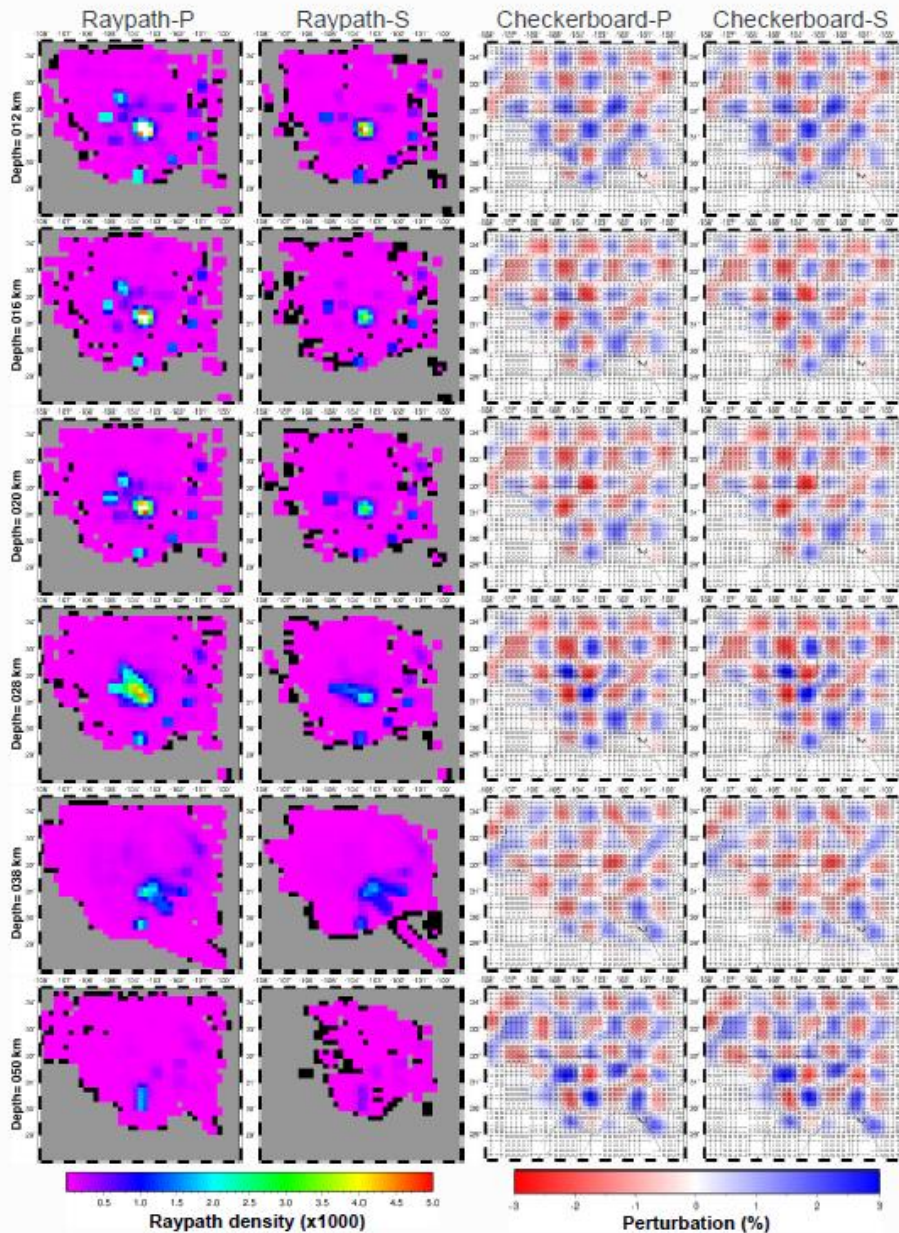


**Figure 6.** Trade-off curve and histograms of traveltime residuals. Note relationship between reduction of RMS traveltime residuals and model adjustments (with respect to starting model for both  $V_p$  and  $V_s$ ) for the inversion. Number above each white circle = iteration number. Top eight insert panels = statistic of traveltime residuals for P- and S-arrivals at 5th, 15th, 29th, and 40th iteration, in which black lines = residuals from the starting 1-D model. Trade-off can be seen between traveltime-residual reductions and model-parameter variations. When both amount of residual reduction and amount of model variation from two consecutive iterations start getting smaller, tomographic inversions are complete. Even though damping factor is dynamically optimized for each iteration, data misfit has been improved sufficiently, and we consider the inversion complete at the 29th iteration.



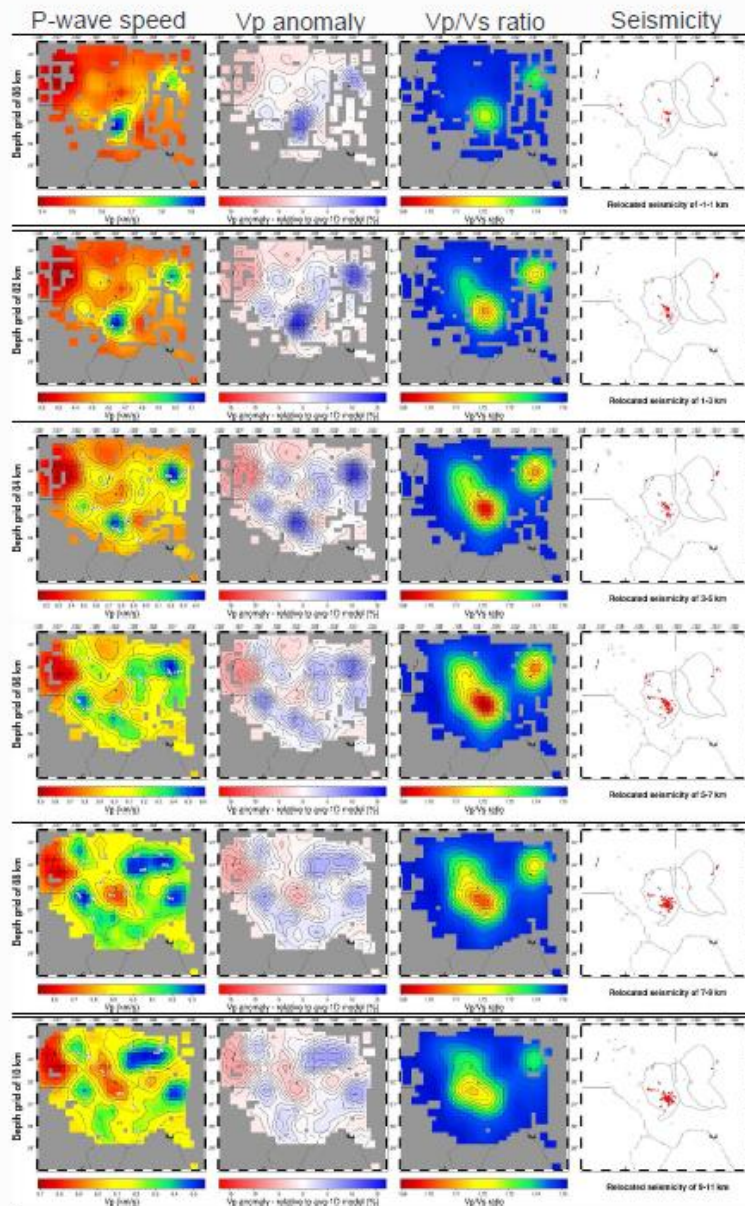
a



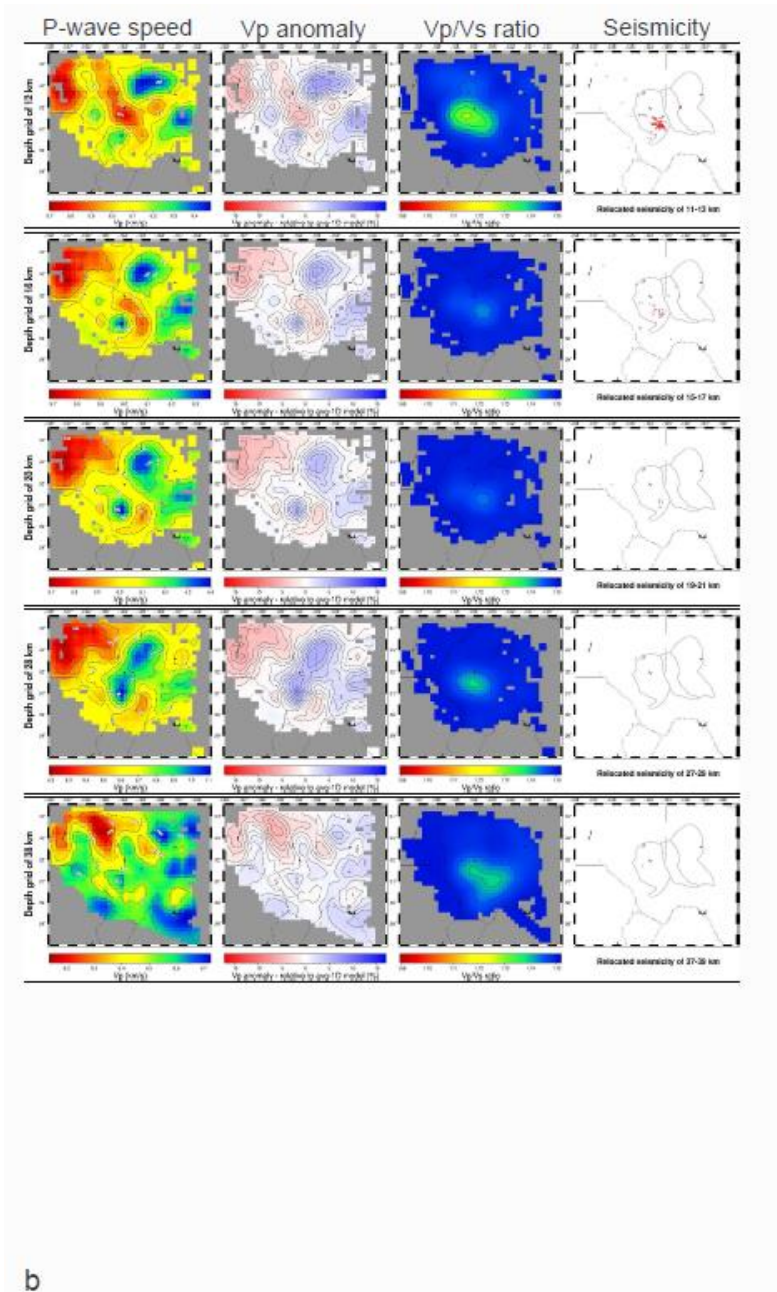
**Figures 7a and 7b.** Assessment of model resolutions in map views at various depths. **(Left two columns)** Raypath-density distribution for both P- and S-waves. Higher raypath densities concentrated in the Delaware and Midland Basins, whereas gray areas = nodes having no passing seismic ray. Black nodes = those having only one passing ray. Higher raypath densities can be seen down to ~30 km depth. **(Right two columns)** Map views for results of checkerboard test at various depths. Crosses and squares = +3% and -3% perturbation in tomographic model as benchmarks to compare. In general, model parameters can be well resolved within the crustal range (to depth of 38

*km) in the study area. At the same time, they are less well resolved but still reasonably constrained to depths of 38–50 km within the study area. Lastly, parameters are poorly resolved below 50 km depth and for areas outside the United States.*

Accepted Article



a



**Figures 8a and 8b.** Map views of P-wave speed, Vp-anomalies (with respect to the 1-D average out of the preferred 3-D tomography model), Vp/Vs ratios, and relocated seismicity at various depths (e.g., 0, 2, 4, 6, 8, 10, 12, 16, 20, 28, and 38 km). Gray color in each panel shows the inversion grids having a number of passing rays less than two; black dashed lines in the panels of seismicity = surface traces of three subunits of the Greater Permian Basin (see Figure 1). Contours in panels of P-wave speed = isopach line in an increment of 0.1 km/s. Contours in panels of Vp anomalies = isopach line in an increment of 1. Contours in panels of Vp/Vs ratios = isopach line in an increment of  $5e^{-3}$ . Seismicity

*shown in each panel is within the depth range of +/- 1 km of the inversion's vertical grid. See text for detailed interpretation.*

Accepted Article

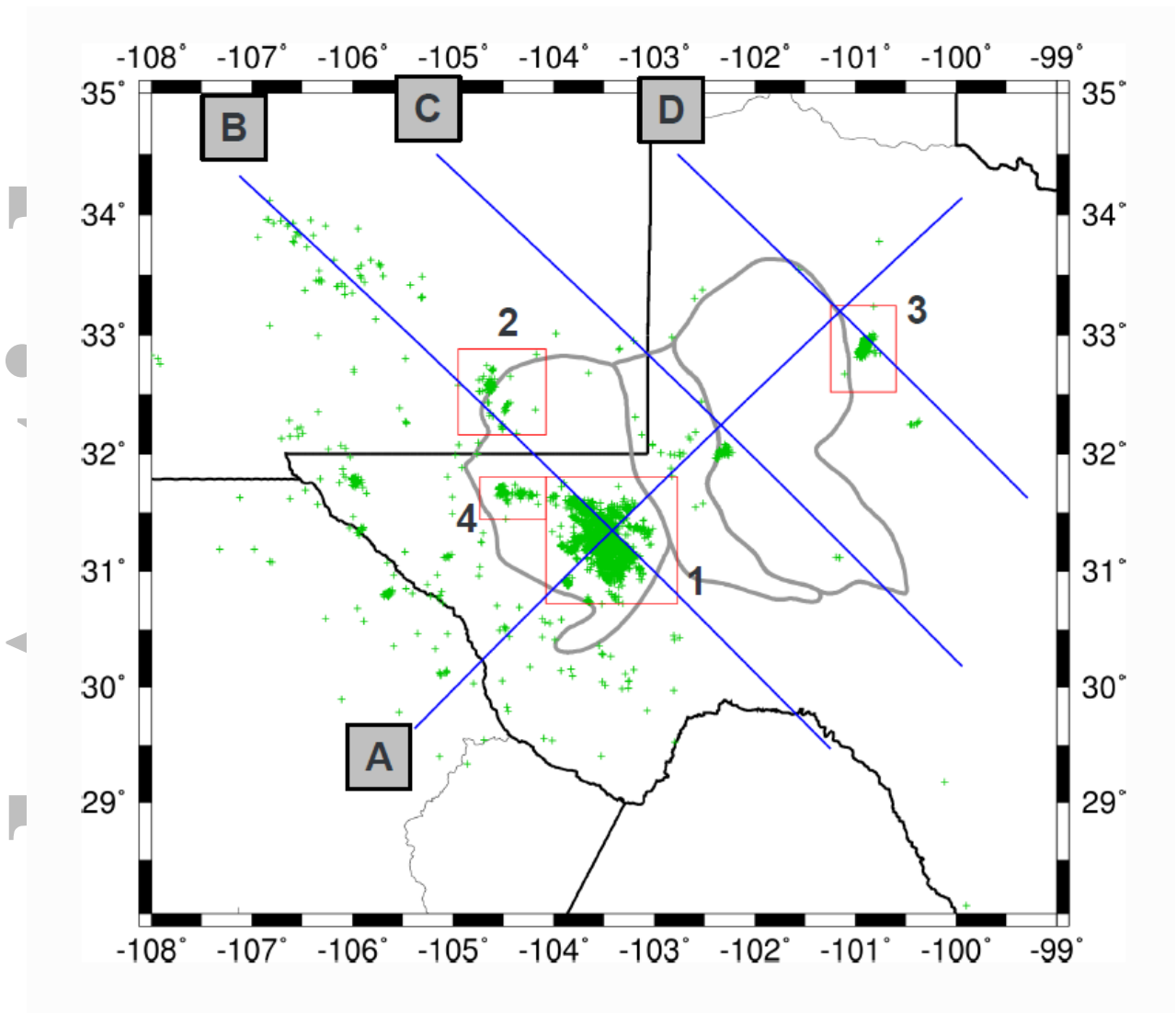
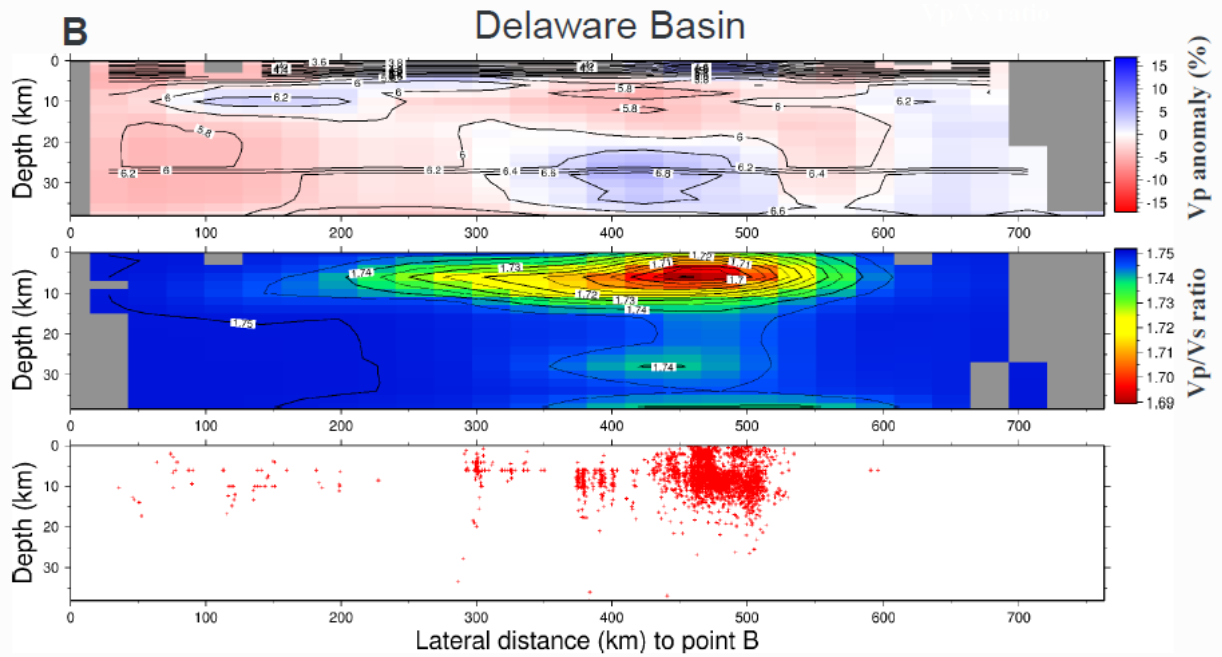
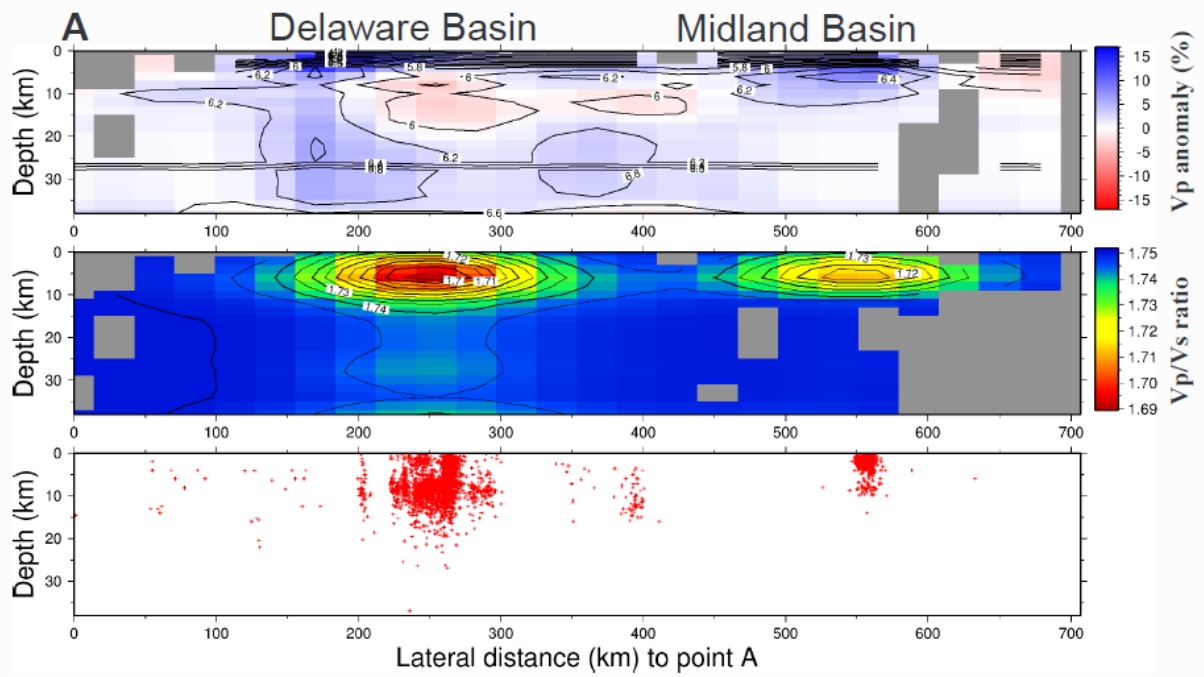
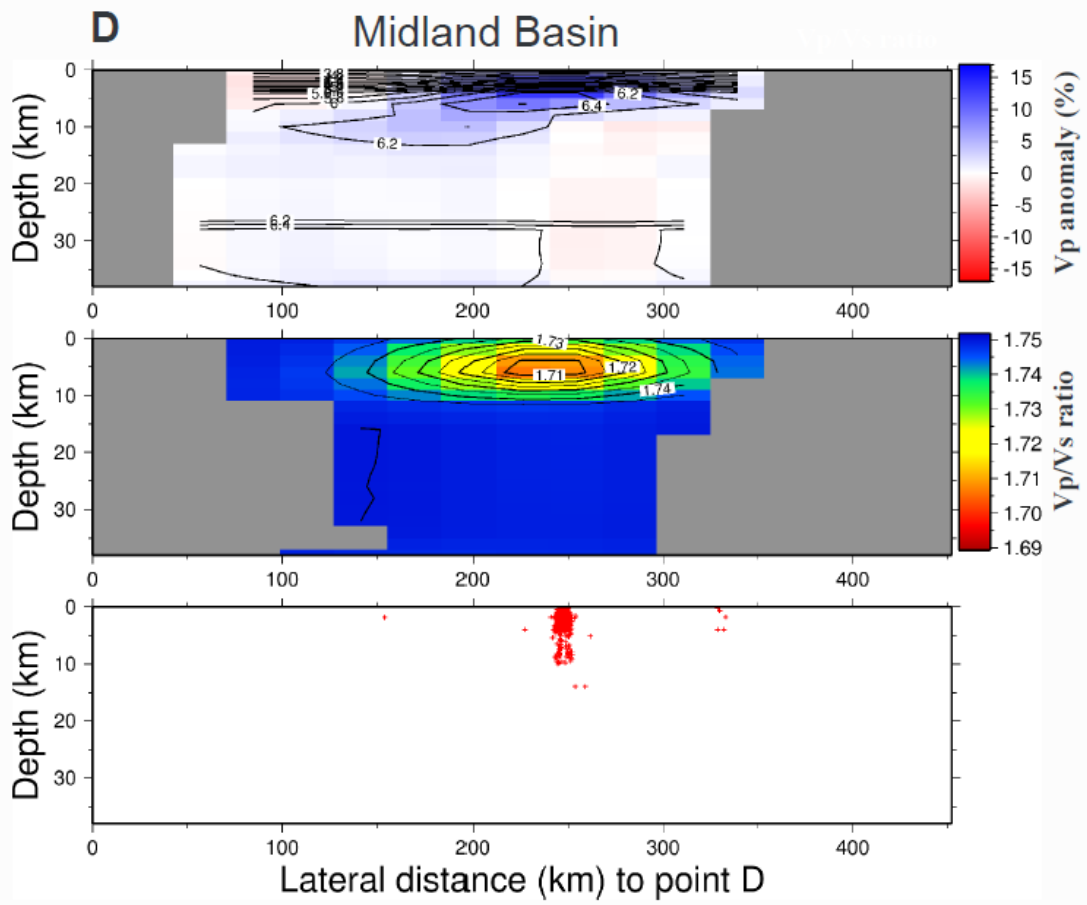
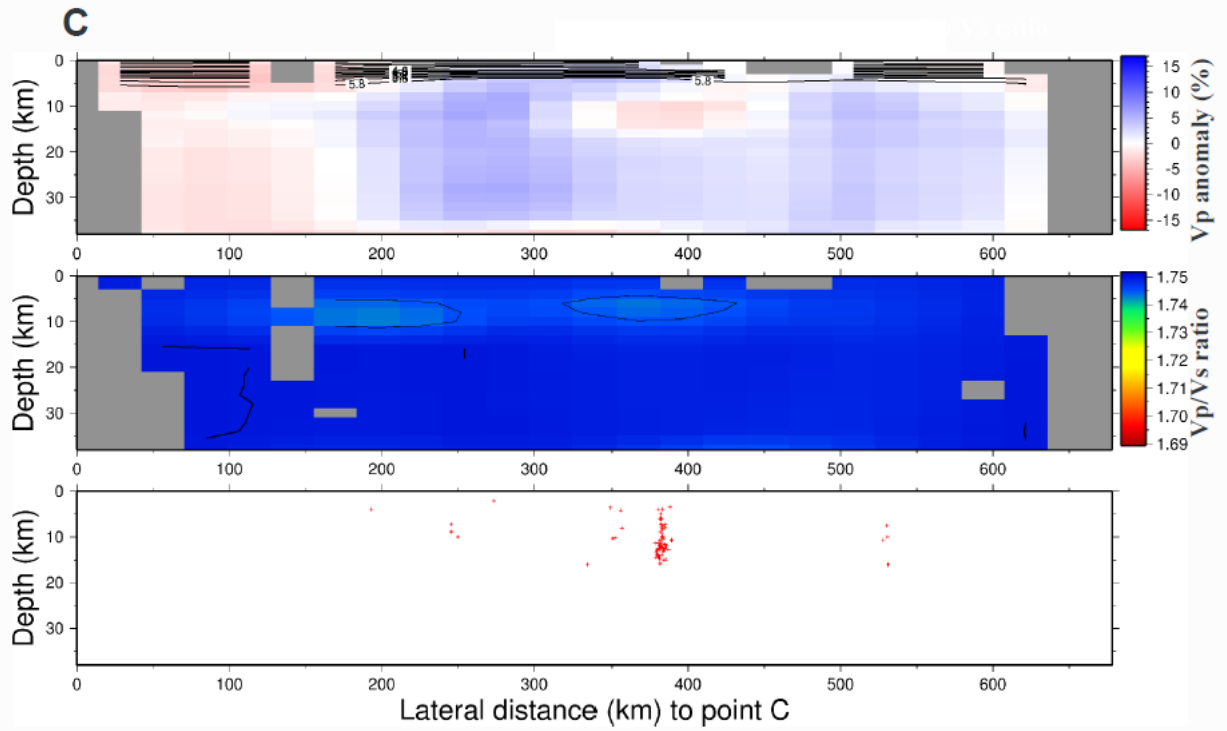


**Figure 9.** Relocated epicenters (green crosses) resulting from tomographic inversion. Blue lines = lines of cross sections shown in Figures 10a–10d. Red lines bracket four major earthquake clusters in the Greater Permian Basin. See text for detailed interpretation.

Accept



Acc



**Figures 10a–10d.** *Four cross-section views of  $V_p$  anomalies (with respect to the 1-D average out of the preferred 3-D tomography model),  $V_p/V_s$  ratios, and relocated seismicity. Depth scales exaggerated ( $H:V = 1:3$ ). See Figure 9 for locations of cross sections. Contours shown in panels of wave-speed anomalies =  $P$ -wave speed, used as proxy to estimate possible lithological boundaries. Significantly lower  $V_p/V_s$  ratios shown in a depth range of 0–10 km in cross sections A, B, and D. The shape of the area having lower  $V_p/V_s$  ratios suggests basin-scale structure that also corroborates regional geology in the study area. Refer to text for detailed interpretation.*

Accepted Article

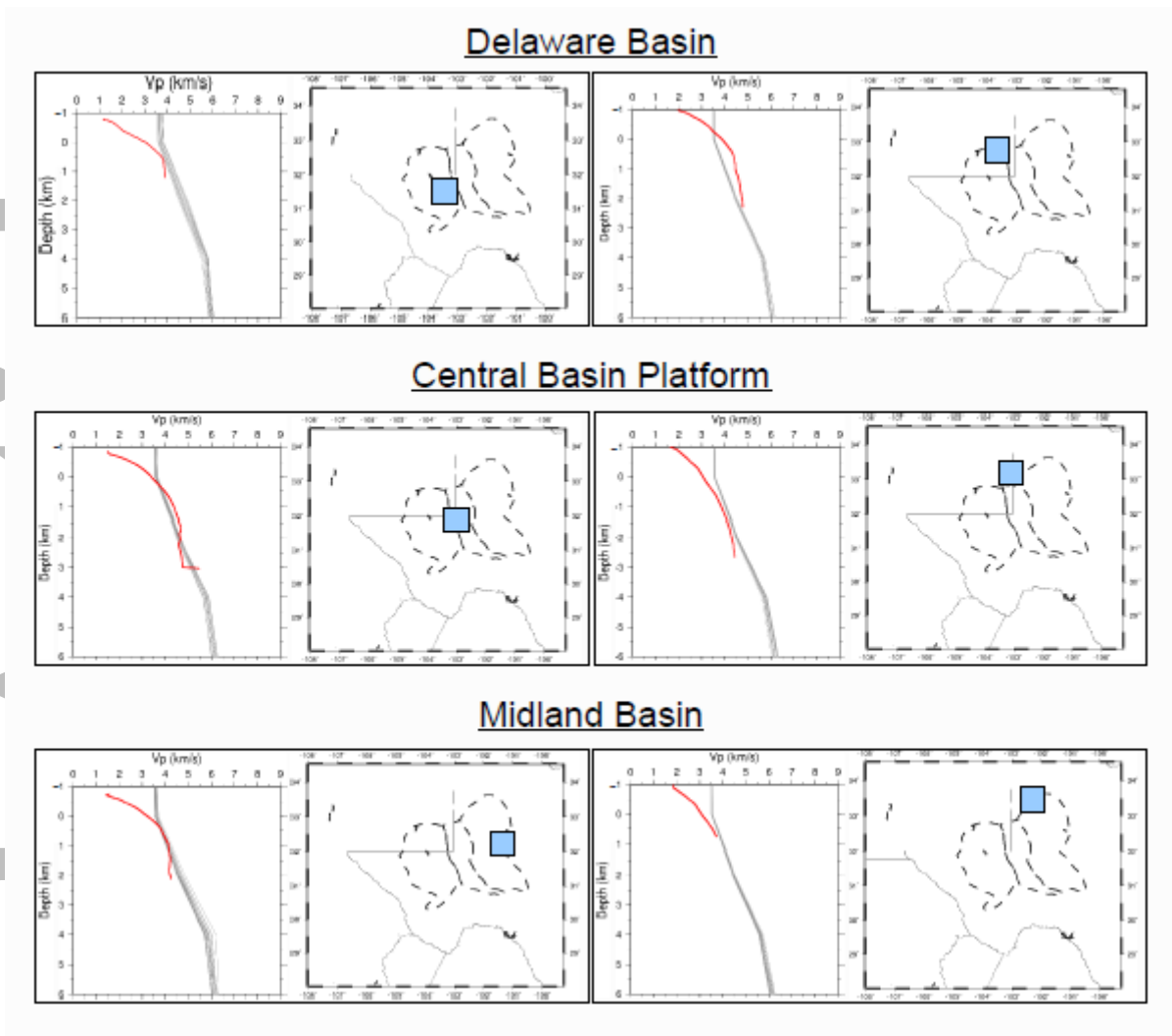


**Figure 11.** Comparison between tomographic wave-speed profiles from this study and vertical seismic profiles from the oil and gas industry. Black dashed lines = surface traces of three subunits of the Greater Permian Basin, whereas blue squares = areas where seismic measurements were taken. Red lines = measurements from vertical seismic profiles, and gray lines = tomographic velocity profiles extracted from area surrounding seismic logging well. Overall, in depth range below 0 km, wave-speed gradient patterns between vertical seismic and tomographic profiles are similar.

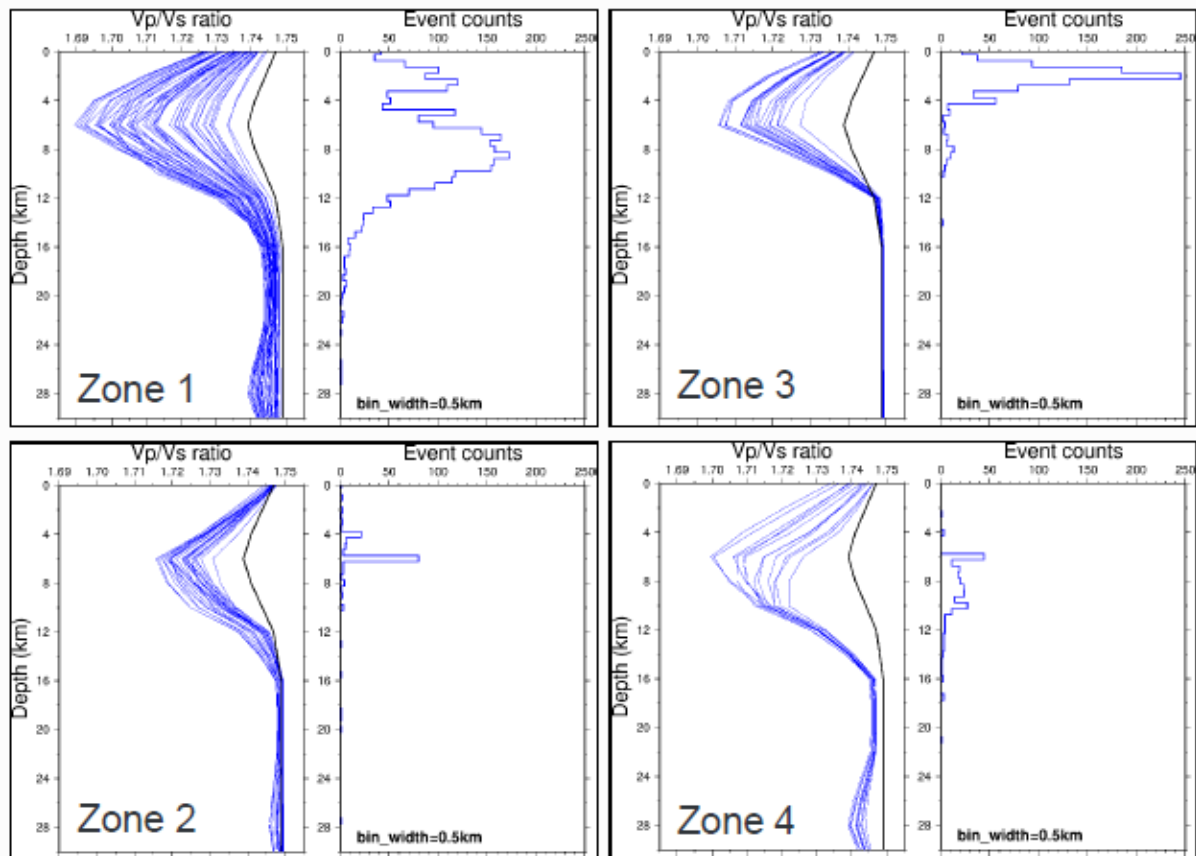


**Figure 12.** Correlation of  $V_p/V_s$  ratios and earthquake distribution in four seismicity clusters. Left part of each panel = vertical profiles of  $V_p/V_s$  ratios of nodes (blue lines). Black line = average  $V_p/V_s$  ratios from study area. Zone 1 has lowest  $V_p/V_s$  ratio (as low as 1.689 at 6 km depth) in study area. Right part of each panel = earthquake counts in the cluster. Event distribution ranges differ in four seismic zones—zone 1 has wide depth range from subsurface to 20 km depth; zone 2 has depth range between subsurface and 12 km depth with a high concentration at 6 km depth; zone 3 has events highly concentrated in range above 6 km depth. Zone 4 has earthquakes clustering below 6 km depth. Highly concentrated earthquake cluster correlates with presence of lower  $V_p/V_s$  ratios in the four clusters. See text for detailed interpretation.

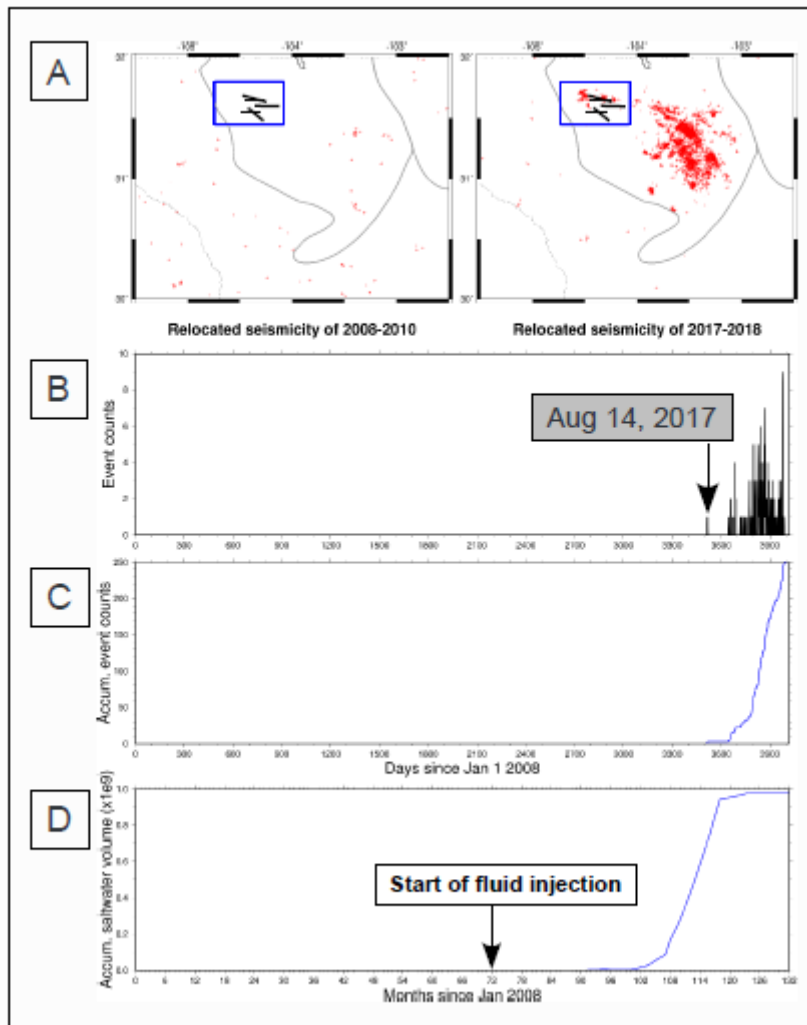


**Figure 13.** Seismicity, state of maximum horizontal stress, and statistic of saltwater disposal for West Texas. Panel A: Zoom-in map view of seismicity of 2008–2010 and 2017–2018 in zone 4 shown in Figures 10 and 12, Black lines in the blue boxes = regional stress (i.e.,  $SH_{max}$ ; Snee & Zoback, 2018); Panel B: Daily counts of earthquakes from January 1, 2008, to December 31, 2018; Panel C: Accumulative counts of earthquakes in zone 4 from January 1, 2008, to December 31, 2018; Panel D: Accumulative volume (in U.S. gallons) of saltwater disposal in zone 4. The data were archived by the Bureau of Economic Geology, with support from the Railroad Commission of Texas. See text for detailed interpretation.